Experimental investigation of the effect of quenching cycles on the physico-chemical properties of granites

Thomas Junique, Patricia Vazquez, David Benavente, Céline Thomachot-Schneider, Yves Géraud

Experimental Investigation of the Effect of Quenching Cycles on the Physico-chemical Properties of Granites

Thomas Junique[1], Patricia Vazquez[1], David Benavente[2], Céline Thomachot-Schneider[1], and Yves Géraud[3]

[1]GEGENAA EA 3795, University of Reims Champagne-Ardenne, 2, esplanade Roland Garros, 51100 Reims, France

[2]Department of Earth and Environmental Sciences, University of Alicante, 03690 Alicante, Spain

[3]GeoRessources Laboratory UMR 7359, University of Lorraine, F54505 Vandœuvre-lès-Nancy

Abstract:

In this study, the physicochemical properties of granitic rocks subjected to quenching cycles were studied experimentally. Four granites of similar mineralogy but with different degrees of initial weathering (porosity between 1 and 6%) were slowly preheated at two peak temperatures (200 and 400 °C) and then quenched 35 times.

To study the effect of thermal cycling on the physical properties, non-destructive tests were used such as water porosity, capillary water absorption tests, P- and S- wave propagation velocities, nuclear magnetic resonance relaxometry, and X-ray micro-tomography. Chemical analysis of the granites was performed using X-ray fluorescence, which provided information on the major and trace elements. Water-granite interactions were followed using inductive plasma mass spectrometry (ICP-MS).

The variation of all the measured parameters indicates the creation of cracks with thermal fatigue. The porosity, water uptake, size, and volume of cracks increased while P- and S- wave velocity and Young's modulus decreased. At 200 °C, the changes were progressive up to ten cycles, from which the stress threshold was reached and only small readjustments took place. At 400 °C, the greatest damage was observed during the first five cycles. These changes were a direct consequence of the propagation of the microcracks induced by the strong gradient during the quenching tests. For both temperatures, the changes depended on the initial weathering conditions of the granites. Initially, weathered granites showed crack development or crack closure during quenching, meanwhile the damage on the sound rocks was characterized by the creation of intragranular microcracks.

The analysis of the experimental fluids showed an enrichment in K, Na and Ca in the solution as consequence of the dissolution of K-feldspar, plagioclase and the degradation of mica and clays, independently of the physical and mechanical modifications.

Keywords: Granites; Thermal cycling; Quenching; Thermal cracking; Microstructural analysis

1. Introduction

Recent environmental awareness is leading the world towards an ecological transition that requires exploring new renewable energy resources. Among them, geothermal energy is a clean, sustainable energy source with abundant reserves and with enormous potential for electricity generation, but its technical and geological feasibility must be well understood before any production. Enhanced Geothermal Systems (EGS) are man-made reservoirs created by drilling wells in a crystalline massif to access hot rocks in the earth's crust. The injection of cold water into the drilling of the EGS produces an overall rapid cooling of the neighbouring rocks. Hot water vapor reaching the surface turns a turbine to generate electricity. The water after being cooled is returned to the well, which subjects the well to repeated heating-cooling cycles (thermal cycles). These cycles allow to stimulate the geothermal energy reservoir. Thermal stimulation is a reservoir permeability enhancement technique prompted by injecting cold water into a reservoir at high temperature (Flores et al., 2005; Siratovich et al., 2011; Tarasovs and Ghassemi, 2012). The beneficial effect of this process is the initiation and propagation of hydraulic fractures created artificially in rocks of low thermal conduction and composed by minerals with high thermal dilation coefficient, such as granite (Kumari et al., 2018). Fluid flow is improved allowing increased thermal energy production. At the crystal scale, the changes in the geometry of the porous network induced by the mineral shape modification can increase or decrease the flow of fluid in the rock (Takarli and Prince-Agbodjan, 2008). The cracks formed in the reservoirs can expand and bring about changes in the physical and mechanical properties of the surrounding rocks. When the crack propagation reaches a certain degree, the stability of the well may change (Bérard and Cornet, 2003; Kumari et al., 2017b; Siratovich et al., 2016). In some areas of a granite reservoir, the thermal gradient can be high and reach 100 °C·km^{-1} (Baldeyrou-Bailly et al., 2004). EGS are typically systems with temperatures of around 200 °C (Olasolo et al., 2016) although some well temperatures, such as Northwest Geysers (California), are measured at 400 °C. These geothermal systems present a great variety in their environment (temperature, hydrology, geomechanics or petrology) although granite is the primary source rock (Breede et al., 2013). Microcracking can start in granite at around 100-120 °C (Junique et al., 2021; Lin, 2002) but most mineral crystals are micro-cracked at around 400 °C (Chaki et al., 2008).

Granite is a low porous and strong material although very sensitive to the effects of temperature. The mineral composition of a granite, the size and grain distribution are major factors that greatly influence mechanical decomposition (Géraud, 1994; Gómez-Heras et al., 2006; Hall and André, 2003; Yilmaz et al., 2009). The increase in temperature will expand the granite minerals. This variation in

volume will be different depending on the nature of the grains (Albissin and Sirieys, 1989; Berest and Vouille, 1988). This differential expansion may lead to irreversible microcracks (intergranular and intragranular), generated above a certain temperature threshold (David et al., 1999; Fredrich and Wong, 1986; Junique et al., 2021; Vazquez et al., 2011, 2015). For the most of the studies, the granites were heated to a given temperature although the monitoring experiments were carried out at room temperature after slow cooling down (Chaki et al., 2008; Gautam et al., 2018; Geraud and Gaviglio, 1990; Kant et al., 2017; Reuschlé et al., 2006; Xu et al., 2008). Some studies monitor the possible microcracking during heating by means of acoustic emission or P wave measurements (Glover et al., 1995; Griffiths et al., 2018). In recent years, more researches have been focused on property changes in the rock after experiencing rapid heating-cooling. For example, Pedras Salgadas granite initially heated to 200 °C exhibits a decrease in flexural strength when cooled with water after a cycle (Lam dos Santos et al., 2011). Wu et al. (2019) show that water-cooled samples exhibited a large decrease in P wave velocity and a large number of newly generated cracks on the sample surface. After having subjected a granite to a succession of 20 quenching cycles between 250 and 650 °C, it has been shown that the damage, followed by a decrease in the P wave velocity, increased with temperature and thermal shock cycles (Dong et al., 2020). Xu and Sun (2018), reported that wave velocity decreases as the temperature increases for the same quenching cycle and the wave velocity has a weaker relationship for more than five quenching cycles. Li et al. (2020) show on thermal shock cycles that the wave velocity and the elastic modulus decrease with an increase in temperature and that when the temperature is above 300 °C, the pre-existing microcracks expand and eventually develop into larger cracks. Yu et al. (2020) carried out 20 cycles of thermal shock at 300 °C and showed a progressive decrease in the peak strength and elastic modulus with increasing cycles.

Water penetrates into the pre-cracked granite through micropores and microcracks, which weakens the cohesive force between the crystals and intensifies the development of cracking (Kumari et al., 2017a). In addition, rapid cooling with water on heat-treated granites induces greater damage than slow cooling, due to thermal gradient cracking (Isaka et al., 2018; Shao et al., 2014). Thus, the permeability of slowly cooled samples increases very weakly at 400 °C, 2.3 times at 500 °C and 35.6 times up to 600 °C while the permeability of fast quenching samples increases 2.9 times at 400 °C, 15.3 times at 500 °C, or even 79.3 times at 600 °C (Jin et al., 2019). The cracking development during these quenching treatments results in a significant reduction in the strength and elastic parameters of the granite as well as in the physical properties due to an augmentation of crack density (Kumari et al., 2017b; Li et al., 2020). Besides, the effect of cyclic heating-cooling leads to a degradation of

rock prompted by the generation and development of micro-cracks (Dong et al., 2020; Kim et al., 2014; Xu and Sun, 2018; Zhu et al., 2020).

Geothermal reservoirs present different range of porosity due to damage (microcracks and alteration) (Surma and Geraud, 2003; Zeng et al., 2017) and the role of the initial microstructure on rock cracking is not clear. As a typical heterogeneous material, granites are prone to behave differently depending on their initial state of weathering. Furthermore, the generation of cracks increases the flow performance (Jin et al., 2019; Kumari et al., 2018; Siratovich et al., 2015). An estimate of permeability is therefore essential for applications in the exploitation of unconventional energy and must be correlated with its damage.

Under the thermal effect of quenching, various chemical changes take place in the internal composition of rocks. Many studies in the literature have followed the physical or mechanical properties of granite, however, only a few studies have incorporated the geochemical interaction into the characterisation of cracking processes (Alt-Epping et al., 2013; Baldeyrou-Bailly et al., 2004; Wogelius et al., 2020). Chemical weathering studies after a fluid-rock interaction are often experiments performed on a single mineral phase, and few studies characterise total mineralogical changes in crystalline rocks (Drüppel et al., 2020; Schmidt et al., 2018).

The main objective of this study is to evaluate the evolution of the granite's void network when exposed to a succession of quenching and the influence of their initial microstructure. For that, four granites with similar mineralogy but with porosity values between 1 and 6% were tested. To obtain an accurate assessment of the sample evolution, a wide range of non-destructive techniques were used to characterise the microcracking distribution, elastic, mechanical and water transport properties, including water porosity, capillary water absorption tests, ultrasounds, nuclear magnetic resonance (NMR) relaxometry, and X-ray micro-tomography (X-ray CT). Finally, the geochemical interaction between water and minerals after thermal cycling was assessed using inductively coupled plasma mass spectrometry (ICP-MS).

2. Materials

2.1. Characterisation of the outcrop samples: geological background

In this investigation, we selected Albero (A), Gris Alba (GA), Golden Ski (GS), and Silvestre Moreno (SM) granites from the Iberian Peninsula (Fig. 1a) due to their similar mineralogy and crystal size and their difference in alteration degree and porosity. The ternary diagram compares the studied rocks with granites from Enhanced Geothermal System (EGS) around the world (Fig. 1b).

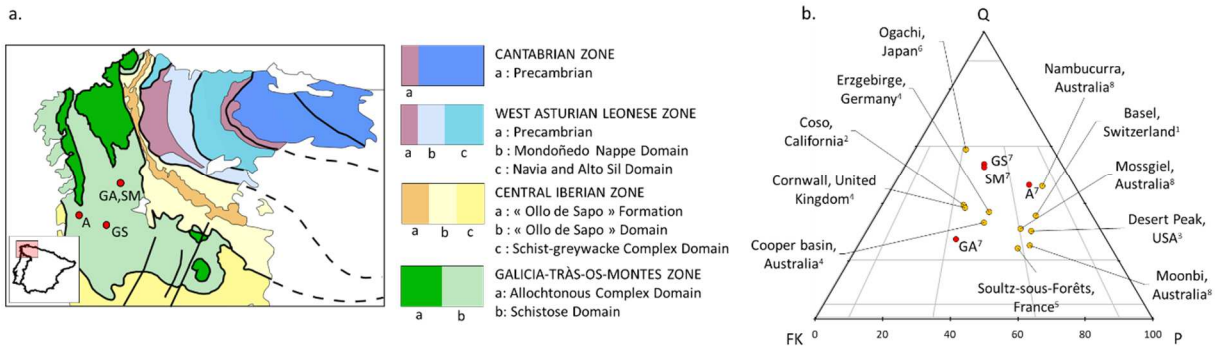

Fig. 1: a. Geological and geographical settings of the Iberian granites studied within the diagram of the Macizo Ibérico : Albero (A), Gris Alba (GA), Golden Ski (GS), and Silvestre Moreno (SM) granites. b. Ternary diagram with quartz (Q), potassium feldspar (FK), and plagioclase (P) representing granites of this study (red) and granites from global EGS sites (yellow). (Alt-Epping et al., 2013[1]; Kovač et al., 2004[2]; Lutz et al., 2004[3]; Marshall et al., 2010[4]; Stussi et al., 2002[5]; Ueda et al., 2005[6]; Vazquez et al., 2018[7]; Zhou et al., 2016[8]).

The granites of this study come from quarries located in the Galician region (north-west of Spain) and the north of Portugal. The granites are located geologically in the Iberian massif and mostly structured during the Hercynian Orogenic Belt formation. All the rocks are post-kinematic and syn-kinematic Hercynian granites and they are located in the so-called Galicia-Trás-Os-Montes area (Farias et al., 1987). The region is sequentially organised into three groups according to their compositional characteristics and structural criteria (Vera, 2004): calc-alkaline syn-kinematic granites, peraluminous syn- and post-kinematic granites, and calc-alkaline post-kinematic granites. The four studied granites belong to the group of Peraluminous syn and post-kinematic granites. This group includes granites temporally related to the processes of regional metamorphism and of Hercynian crustal anatexis. Albero is in Donón-Tomiño alignment which represents an elongated mass of about 56 km and 12 km wide with a small deformation that gives orientation to the minerals. This formation of longitudinal axis is parallel to the general directrices of the Hercynian in this region of Galicia. In 2004, the Geologic and Mining Spanish Institute (IGME) described the Gris Alba and Silvestre Moreno varieties as "very leucocratic two-mica granites". They are found in the Salvaterra-A Cañiza-Cerdedo alignment, which belongs to the Faro de Avión batholith. This massive elliptical shape measures about 7.5 km by 4 km. The Golden Ski variety places within the Salvaterra–A Cañiza–Cerdedo Alignment, which is an elongated granitic batholith with the longitudinal axis parallel to the general guidelines of the Hercynian in this area of Galicia.

2.2. Granite description

Binocular and microscopic views of the studied granites are shown in Figure 2. The petrographic characterisation (mineral proportion and crystal size) was produced by Vazquez et al. (2018) by optical polarising microscopy and the main petrographic characteristics are presented in table 1.

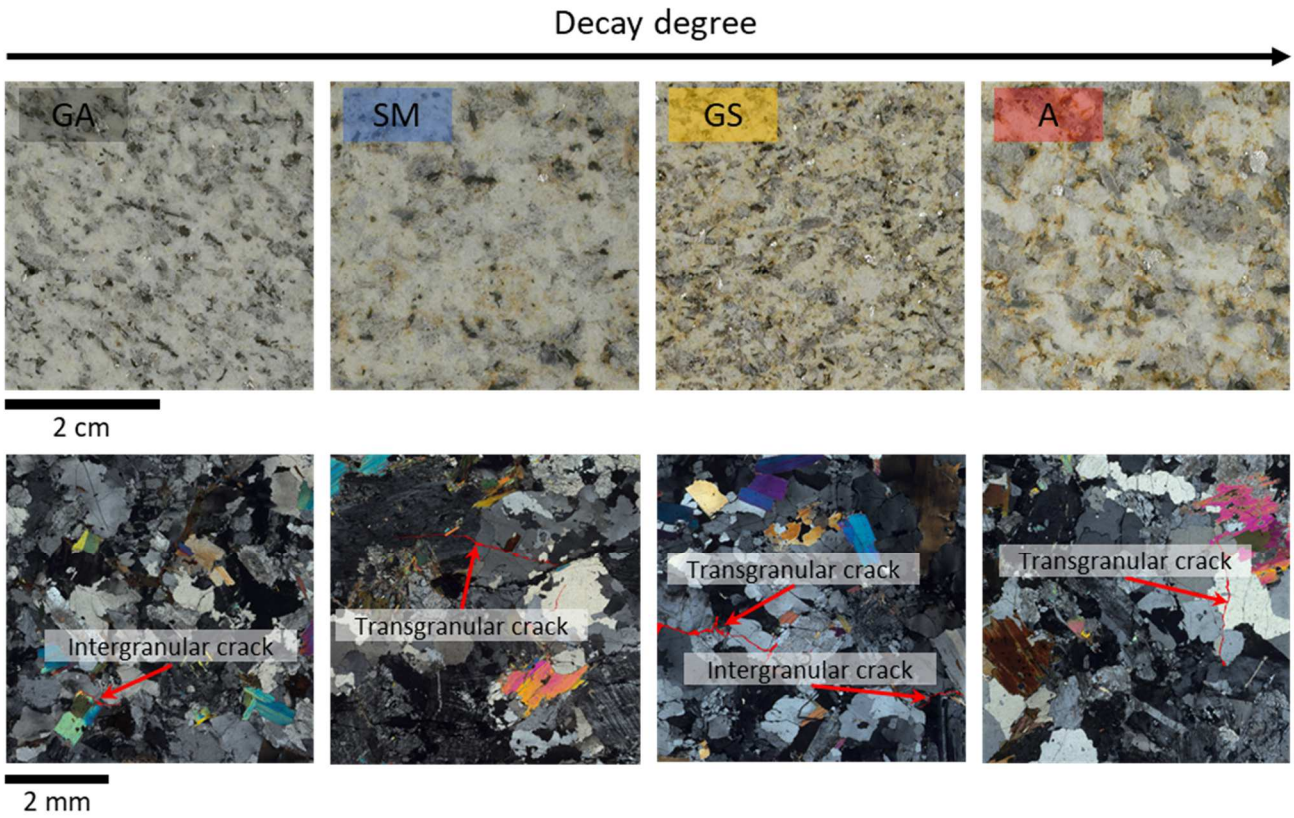

Fig. 2: Macroscopic and microscopic photography of the studied granite: Gris Alba (GA), Silvestre moreno (SM), Golden ski (GS), and Albero (A).

Tab. 1: Characteristics of the selected granitoids. Trade name, mineral proportion (studied using optical polarisation microscopy), IUGS classification (Le Maitre, 2002) and the crystal size of the studied granites (Vazquez et al., 2018). (Avg.: Average; Q: quartz; FK: alkali feldspar; P: plagioclase; M: mica).

	Composition (%)					Crystal size (mm)				
Stone	Q	FK	P	M	IUGS classification	Q	FK	P	M	Avg.
A	35	10	30	25	Granodiorite	5	5	6	4	5
GA	23	37	23	17	Monzogranite	5	5	4	2	4
GS	47	20	20	13	Monzogranite	4	4	4	2	4
SM	45	20	20	15	Monzogranite	4	5	7	4	5

Albero (A): The yellowish hue found in the granite was due to a notable initial alteration and the presence of clay. Indeed, this granite was characterised by open transgranular cracks. It was a homogeneous granodiorite with medium-fine crystal (5 mm). It had the lowest alkali feldspar content among the four granites studied and a high proportion of muscovite and biotite (25%). A contains elongated xenomorphic minerals orientated according to the foliation. Most boundaries were interpenetrated.

Gris Alba (GA): The intergranular cracks observed in this granite can be found mainly at the edge of the micas. It was a homogeneous monzogranite with fine crystal (4mm). It had anhedral minerals

178 and the boundaries between the quartz crystals were irregular. The proportion of muscovite biotite
179 minerals was about 2:1.
180 Golden Ski (GS): Pre-existing cracks were of intergranular nature and were present in plagioclases.
181 GS also had open transgranular cracks. It was a homogeneous monzogranite with fine crystal (4
182 mm). Quartz and feldspars were subhedral and muscovite was euhedral. These were the muscovite
183 crystals that have the largest crystal size and plagioclase the smallest crystal size. Quartz content was
184 higher than that of feldspars which is 20% of plagioclases. This granite had an initial alteration
185 characterised by the presence of clay.
186 Silvestre Moreno (SM): Like A and GS, this granite had an initial alteration indicated by the presence
187 of intra, inter and transgranular cracks. It was a homogeneous monzogranite of small size (5 mm).
188 These minerals were subidiomorphic. After GS, this granite had the highest quartz proportion of the
189 granitoids studied. SM had the same proportion of feldspars and plagioclase (20%) as GS.
190 Plagioclases were the minerals with the largest size (7 mm).

191 3. Methodology

192 3.1. Sampling and analytical procedure

193 The experimental method was specifically designed to verify the impact of an abrupt change of
194 temperature in the granites (Fig. 3a) because there are not quenching standard tests.

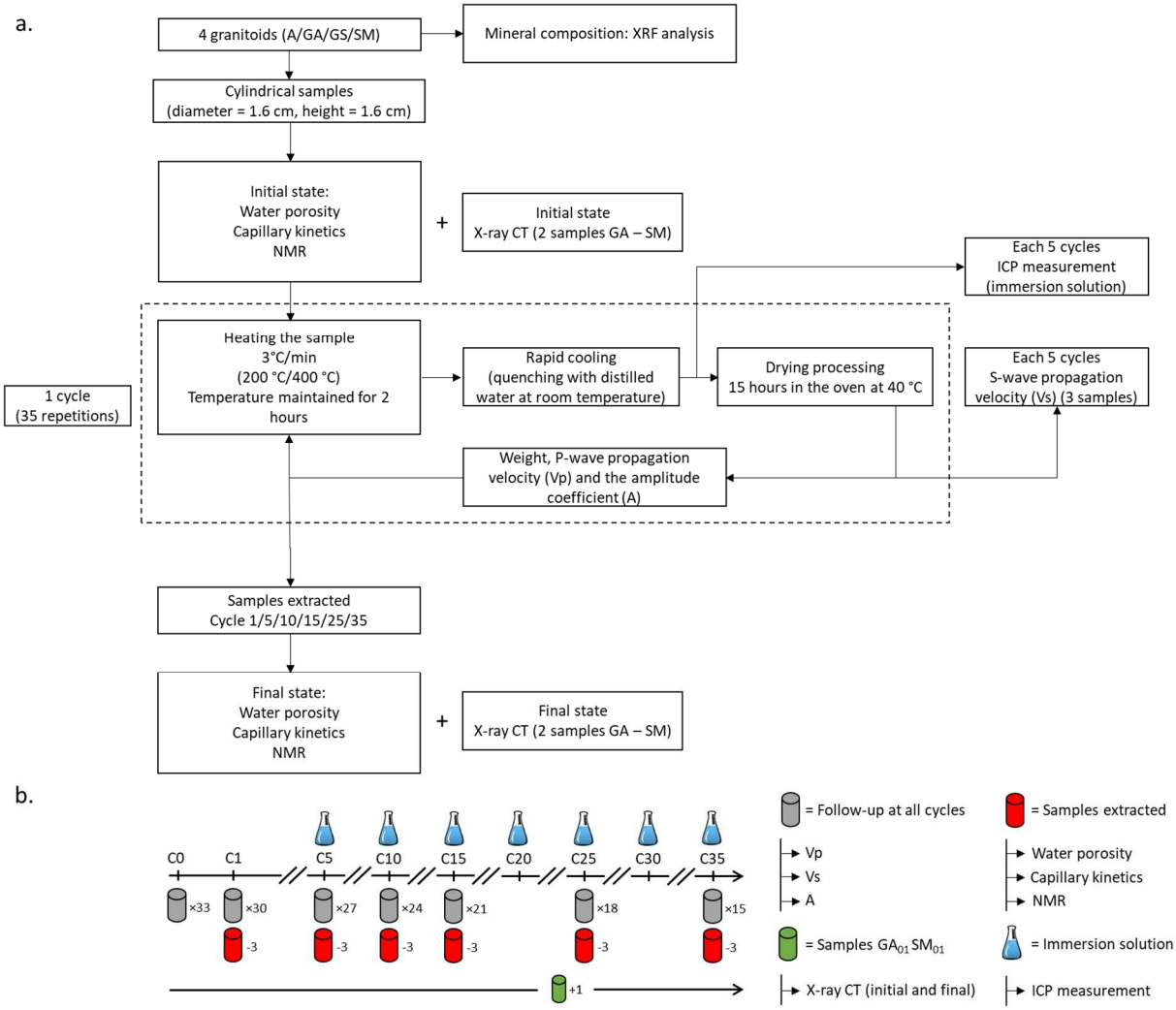

Fig. 3: a. Experimental methodology. b. Detail of sampling during the cycles (C).

The samples are cylinders 1.6 cm in diameter (d) and 1.6 cm in height (h). A total of 33 samples per granite and per quenching test were used. A total of 3 samples per granite were removed on the 1/5/10/15/25/35 cycle for each quenching test. Samples of the purified water (5 ml) used during cooling was removed every 5 cycles for each quenching test (Fig. 3b). The water samples taken will be analysed by inductively coupled plasma mass spectrometry (ICP-MS).

3.2. Thermal treatment

The main goal was to study the influence of cyclic quenching on the mechanical and microstructural properties of granites. The samples were heated at a rate of 3 °C/min until the target temperature was reached. This heating rate was low enough to avoid thermal shocks on the granite and to ensure that induced microcracks were the direct response of temperature and not of the temperature gradient within the sample (Dwivedi et al., 2008; Li et al., 2020; Zhu et al., 2020). Two heating

temperatures (200 and 400 °C) were selected as average and maximum temperatures of existing geothermal systems (Breede et al., 2013). The temperature was kept constant for 2 hours to distribute the assigned temperature evenly (Tang et al., 2019). Cold distilled water (~25 °C) was then instantly inserted into the container containing the samples for 1 hour. This water was changed after each cycle. According to Zhang et al. (2018), the sample surface cooling time was about 10 and 25 min for the heating temperature of 200 and 400 °C. This cycle was repeated 35 times.

3.3. Physical property tests

3.3.1. Water porosity

Connected porosity (φc) is defined as the ratio of the volume of connected voids to the total volume of rock. In this study, the experimental protocol followed the standard NF EN 1936, (2007). It consists of obtaining the porosity using the triple mass method. The dried samples were weighed and placed in a desiccator where the pressure was gradually lowered with a vacuum pump to remove any air from the pores. The degassed distilled water was then gradually introduced until the samples were completely immersed. Once atmospheric pressure was restored, the samples were left in the water for 24 hours. The saturated mass and the hydrostatic mass of the samples were then recorded.

3.3.2. Capillary coefficient

Capillarity on a natural stone is an intrinsic property and represents its ability to absorb water under the effect of capillary forces. This property is directly related to the porous network (size, pore shape, and network connection). The capillary coefficient (C) was calculated based on the NF EN 1925, (1999) standard. The samples were dried at 40 ± 5 °C before each test until their masses stabilised. The principle of experience is to put our porous solid in contact with distilled water. Capillary kinetics are usually characterised by two phases (Hammecker et al., 1993; Hammecker and Jeannette, 1994). The first phase is the progressive filling of the free porosity by the capillary forces of water without external pressure applied. The slope of this curve represents the capillary coefficient (Roels et al., 2000) that is the volume of water penetrated by capillarity into the rock per unit of square root of time according to the Washburn law ($g \cdot m^{-2} \cdot s^{-1/2}$). The restitution curves of the water uptake tests give information about the porous network (Benavente et al., 2015, 2002). The modification of the porous networks of the samples was only assessed through the variation of this parameter.

3.3.3. Elastic rock properties and deduced mechanical properties

P- and S-waves propagation velocities (Vp and Vs respectively) were measured to estimate dynamic mechanical rock properties. Moreover, the monitoring of the ultrasonic signal is effective in evaluating the characteristics of the pores of the rock because if depends mainly on the size, connectivity, and distribution of the pores, the lithology, and the bedding plans. Propagation velocities were measured using equipment for receiving non-transmitting signals (Panametrics-NDT 5058PR) coupled to an oscilloscope (TDS 3012B-Tektronix). The transducer frequency was centered on 2.5 MHz for P-waves and 1 MHz for S-waves. To ensure the transmission of ultrasonic energy between the transducers and the surface of the sample, a visco-elastic coupler was used. Constant pressure was systematically applied between the transducers and the sample. In this study, the P-wave velocity was measured on all the samples after each cycle of quenching. Vs was measured every 5 cycles on 3 samples for each test.

Dynamic Young's Modulus (E) (1) and Poisson's ratio (ν) (2) were calculated as follows (Homand et al., 2000):

$$E = \rho g \frac{Vp^2(1+\nu)(1-2\nu)}{1-\nu} \quad (1)$$

$$\nu = \frac{\frac{1}{2} - (\frac{Vs}{Vp})^2}{1 - (\frac{Vs}{Vp})^2} \quad (2)$$

Where ρg is the bulk density determined through direct measurement of dried weights and dimensions of samples.

In addition to Vp and Vs, the amplitude coefficient (A) was obtained. It was defined as the ratio between the Amp (x) and the Amp (i). Amp is the maximum amplitude (in absolute values) measured in the waveform of the signal received: Amp (i) corresponded to the value of the samples before the tests and Amp (x) after each quenching test.

The quantification of this parameter allowed to estimate textural defects induced to the rock. The presence of an open fracture brings about a strong scattering of the ultrasonic waves and induces a decrease in coefficient A. The attenuation of the signal amplitude (Fig. 4) depends on the textural characteristics of the rock and the individual defects but is less sensitive to crystal size and porosity as may be Vp (Martínez-Martínez et al., 2011).

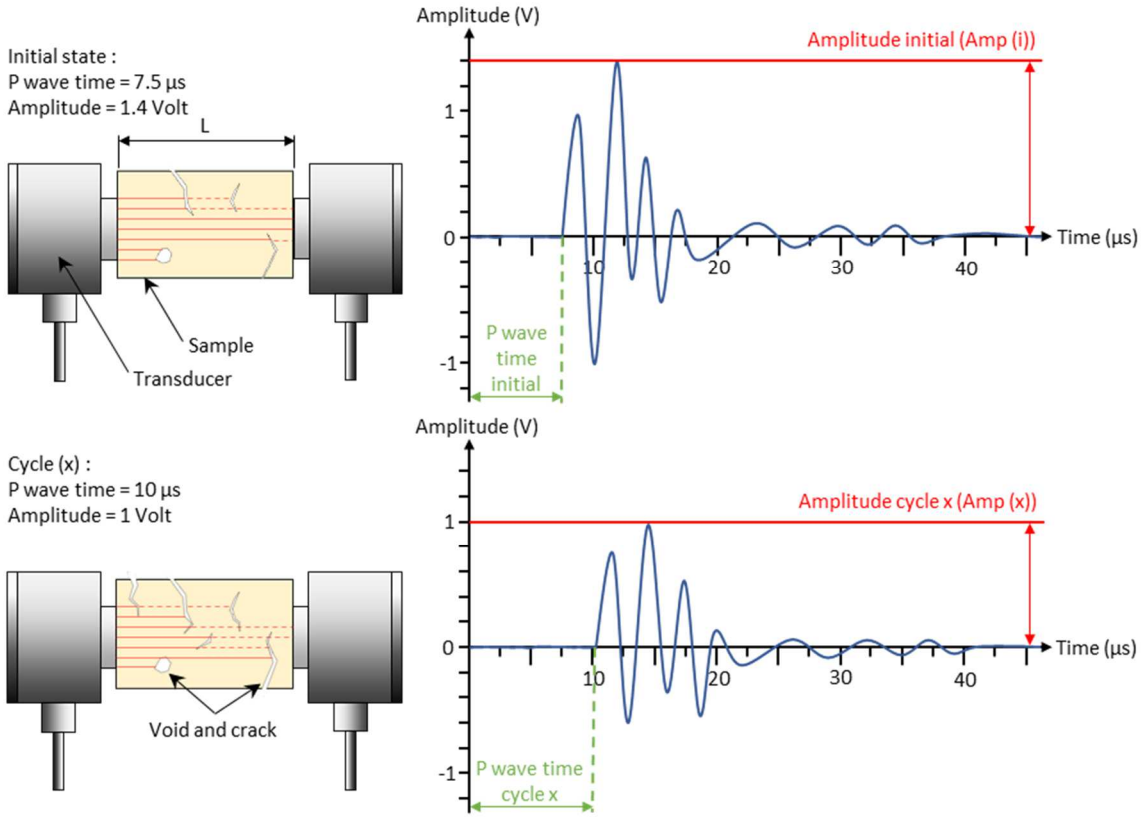

Fig. 4: Diagram of the transmission of ultrasonic waves with an example of signals received as a function of the degradation of the rock.

3.3.4 Nuclear Magnetic Resonance relaxometry

Nuclear magnetic resonance (NMR) is a fast, practical, and non-destructive tool for characterizing complex porous media. The NMR measurements were carried out on a set of 66 samples of each sound granitoid using a minispec mq-Series instrument. NMR is based on the decay by magnetisation of the hydrogen nucleus of water and useful for the deduction of certain information on the structure of pores (distribution pore) (Liu et al., 2017; Tian et al., 2020; Weng et al., 2018). The rock samples were vacuumed and saturated for 24 h and were then soaked in water for 24 h to fill the rock material with water. During the measurement, the sample was taken out from the water and instantly integrated into a hermetic support before being placed in the NMR. That maintained the saturation during the whole measurements. The NMR method estimates the diameter which corresponds to the width between the porous walls (Fig. 5).

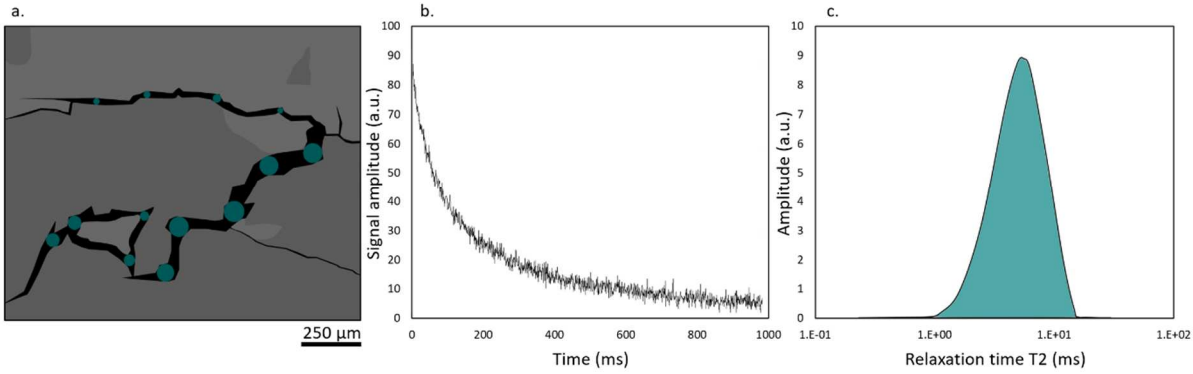

Fig. 5: Summary of the use of NMR in the analysis of porous rocks. a. Diagram of the enlarged 2D X-ray CT view of the SM granite to visualise the cracks, the blue circles are detected by NMR. b. The transverse magnetisation decay curve (example of measurement on the SM granite). c. The transverse relaxation time (T2) distribution curve constructed by a mathematical inversion process (the curve reflects a distribution of pore, surface to volume ratios V/S).

The transverse relaxation time (T2) is measured with a Carr-Purcell-Meiboom-Gill (CPMG) sequence, at regular time intervals 2τ (or TE) of 100 µs. The transverse magnetisation decay curve (Fig. 5b) is the sum of all decay signals generated by the protons in the sample. Dynamics Center software (Version: 2.5.5) was used to represent the distribution of relaxation times (the amplitudes Ai as a function of T2i) obtained through a mathematical transformation (Laplace inverse) (Fig. 5c).

These are the surface effects and the physical properties that are used in nuclear magnetic relaxation in porous media. Each T2 is linked to the porous space of the sample, in particular the ratio/surface.

This link is transcribed in the equation (3) (Fleury, 1998), as follows:

$$\frac{1}{T2} = \frac{1}{T2b} + \rho\frac{S}{V} + \frac{1}{12}(TE\gamma G)^2 D \quad (3)$$

Where T2 represents the transverse relaxation time, ρ is the specific surface relaxivity (of the order of 1-30 µm·s^{-1} for natural porous media). T2b represents the relaxation time of the fluid saturating the porous space (2700 ms for water at 30 °C), S is the surface and V the volume of the pore considered, TE is the inter-echo time of the CPMG sequence; we set it at 100 µs, G is the average local magnetic field gradient, γ is the gyromagnetic ratio and D is the auto-diffusion coefficient of the fluid. The term diffusion can be neglected in equation (3) because T2 is independent of the inter-echo time (very weak in this experiment).

The geometry of our pores must be hypothesised. In the monophasic case, the spherical pores have a surface ratio of:

$$\frac{S}{V} = \frac{3}{r} \quad (4)$$

where r is the pore radius. If we consider that our pores are spherical, we simplified equation (5), as follows:

310 $$\frac{1}{T2} = \frac{1}{T2b} + \rho\frac{3}{r} \quad (5)$$

311 The values of T2 were taken before and after cycling. Thus, the T2 distribution reflects the
312 information on the pore size, the smaller the T2 value, the smaller the pore size.

313 3.3.5. X-ray micro-tomography

314 X-ray microtomography (X-ray CT) is a non-destructive technique that permits to visualise in 3
315 dimension the modifications of the porous network at high resolution, without sample preparation
316 or chemical fixation. As a result, the natural characteristics of the mineralogical information and the
317 porous network have been maintained. X-ray tomography imaging was performed on a Phoenix
318 Nanotom S. A rectangular prisms of size 5 x 5 x 10 mm of the GA and SM granite were analyzed
319 before and after 35 quench cycles. The X-ray tomography scan resolution was associated with the
320 sample size. The resolution was about 1 voxel = 6 µm. The maximum voltage that this
321 microtomograph can supply is 180KV/15W. An X-ray source generates beams which pass through
322 the sample placed on a 360 ° rotating stage, leaving shadow projections on the detector and
323 acquiring several 2D X-ray absorption images (Fig. 6). The measurement of the X-ray attenuation is
324 proportional to the local bulk density of the object if the chemical composition of the object is
325 uniform. Density values are represented by grey levels, black is equivalent to air while white is set to
326 the highest mineral density. In general, feldspar, quartz, and biotite minerals have average densities
327 of 2560 kg·m^3, 2648 kg·m^{3,} and 3090 kg·m^3, respectively. Therefore, biotite will appear in light colour
328 on images scanned by X-ray tomography, and quartz and feldspar minerals will have darker colours.
329 The small difference in density between quartz and feldspar makes their identifications more
330 difficult. The sectional images of the object are reconstructed and allow to create a full 3D
331 representation of the samples. In geoscience, this technique has been widely implemented in studies
332 (Fan et al., 2018; Géraud et al., 1999; Isaka et al., 2019; Kumari et al., 2018; Sepúlveda et al., 2020;
333 Yun et al., 2013).
334

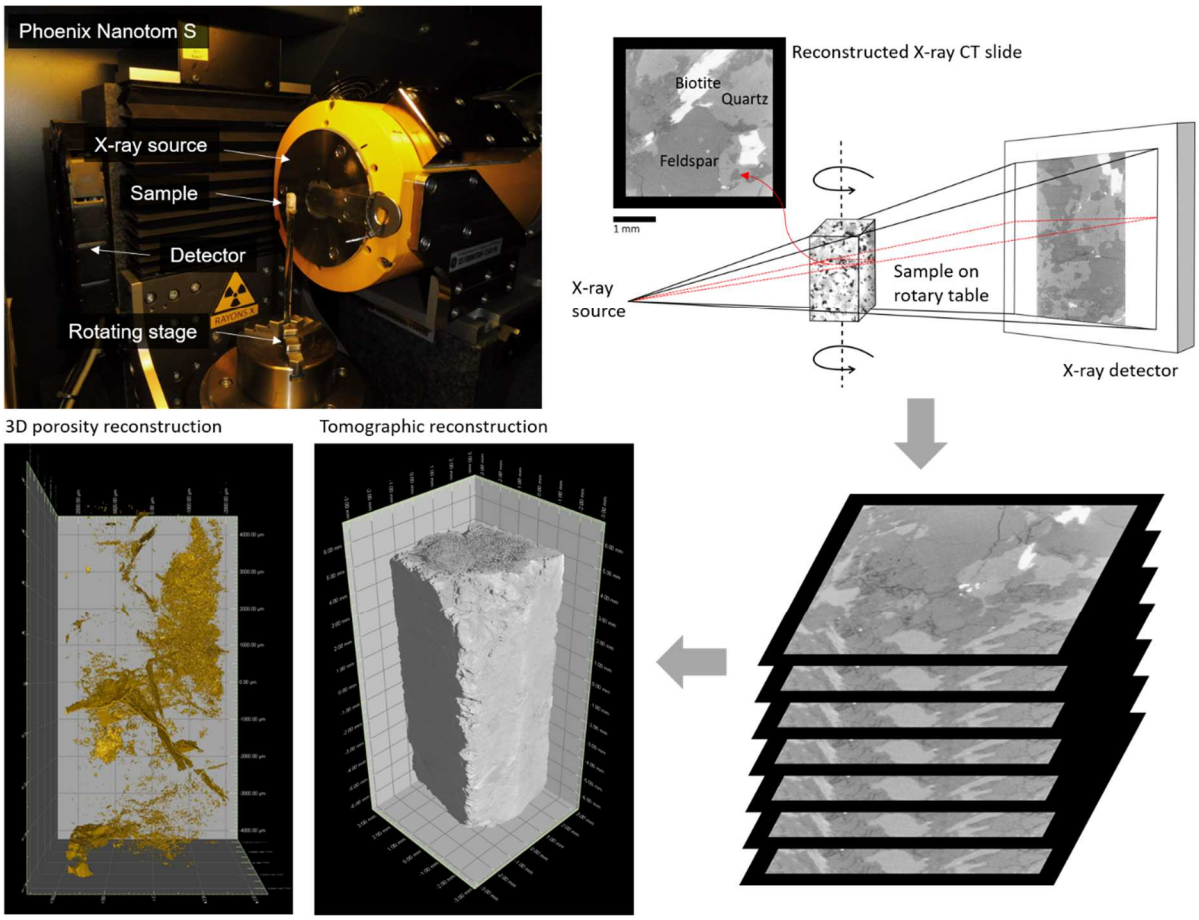

Fig. 6: Principle of X-ray microtomography going from image reconstruction to 3D visualisation.

At the end of the acquisition process, the VGStudio MAX 2.2 © software (Volume Graphics) was used to perform the reconstruction and its qualitative and quantitative analysis. First, the volume defects associated with the acquisition were eliminated. Regions of Interest (ROI) were created respecting the capacity of the computer used and being the most representative of the entire sample. The same ROI was selected on the samples before and after treatment. The segmentation of the images allowed to separate the mineral phase from the crack porosity by attributing to each voxel of the image the corresponding phase according to its shade of grey. The porosity values of the slides were strongly influenced by the choice of the binarisation threshold. For this reason, the adjustment parameters remained the same throughout all the analysis. Different properties of the voxels (volume, diameter, sphericity, etc.) were obtained using a flaw detection tool.

The heterogeneity of the distribution of microcracks along the z height was evaluated. From the porosity of the X-ray CT images of the cross-sections in x – y planes, the coefficient of variation (CV) was calculated before and after the quenching. It is defined as the ratio of the standard deviation to the mean of the porosities of the sections in the xy plane.

3.4. Chemical analysis

3.4.1. X-Ray Fluorescence and Inductively coupled plasma mass spectrometry analysis

The chemical analysis of the granites was performed using X-Ray Fluorescence (XRF) (Philips Magix Pro device), which provided information of major and trace elements.

The geochemical reactivity of the water-granite interaction was carried out by analysing the resulting/lixiviated water after one hour of water-quenching for each granite type and test every 5 cycles (Fig. 3b). The contents of dissolved Al, Ca, Fe, Mg, Mn, Na, K, and Ti were determined using Inductively coupled plasma mass spectrometry (ICP) (VG PQ-ExCell, Thermo Elemental). Nitric acid (HNO_3) was added before analysis to stabilise the solutions.

4. Results

The results of the initial physical properties of the selected stone are shown in Table 2.

Tab. 2: Values of physical properties. φc: connected porosity C: capillary coefficient; Vp: P-wave propagation velocity; Amp: maximum amplitude of the P-waves; Vs: S-wave propagation velocity; E: Young's modulus and T2: transverse relaxation time.

	φc (%)		C ($g \cdot m^{-2} \cdot s^{-1/2}$)		Vp ($m \cdot s^{-1}$)		Amp (V)		Vs ($m \cdot s^{-1}$)		E (GPa)		T2 (ms)	
Stone	Avg.	St.d.	Avg.	St.d.	Avg.	St.d.	Avg.	St.d.	Avg.	St.d.	Avg.	St.d.	Avg.	St.d.
A	5.20	0.48	13.26	2.54	2526	322	$5.6x10^{-04}$	$2.9x10^{-04}$	1066	147	7.93	1.99	10.7	2.0
GA	1.19	0.35	2.39	0.45	3292	118	$8.0x10^{-03}$	$4.1x10^{-03}$	1549	94	17.22	2.07	38.8	4.0
GS	3.75	0.64	14.23	1.00	1758	197	$1.0x10^{-03}$	$4.8x10^{-04}$	889	149	5.30	1.69	25.0	2.8
SM	2.40	0.30	8.92	3.25	3951	308	$4.1x10^{-03}$	$1.7x10^{-03}$	1657	260	20.24	6.42	11.7	2.1

Avg average, St.d standard deviation

The degree of initial weathering of the four granites was assigned relative to their initial porosity.

Albero (A) will be referred to as a highly weathered granite with the highest porosity of 5.2%. Therefore, it showed low Vp and Vs values of about 2526 and 1066 $m \cdot s^{-1}$, respectively. Gris Alba (GA) will be referred to as an unaltered granite with a low porosity of 1.2%. This granite showed the lowest values of the maximum amplitude of Vp. It showed the highest relaxation time T2 values. Golden Ski (GS) will be referred to as a moderately weathered granite with a porosity of 3.75%. It showed a highest C coefficient and lowest value of Vp and Vs of approximately 1758 and 889 $m \cdot s^{-1}$, respectively, resulting in a low value of the elastic modulus E of 5.3 GPa. Silvestre Moreno (SM) will

be referred to as a slightly weathered granite. It showed a porosity of around 2.4% and the highest Vp, Vs and E values.

4.1. Connected porosity

The water porosity was calculated before the test and on the samples removed during the cycles (Fig. 7).

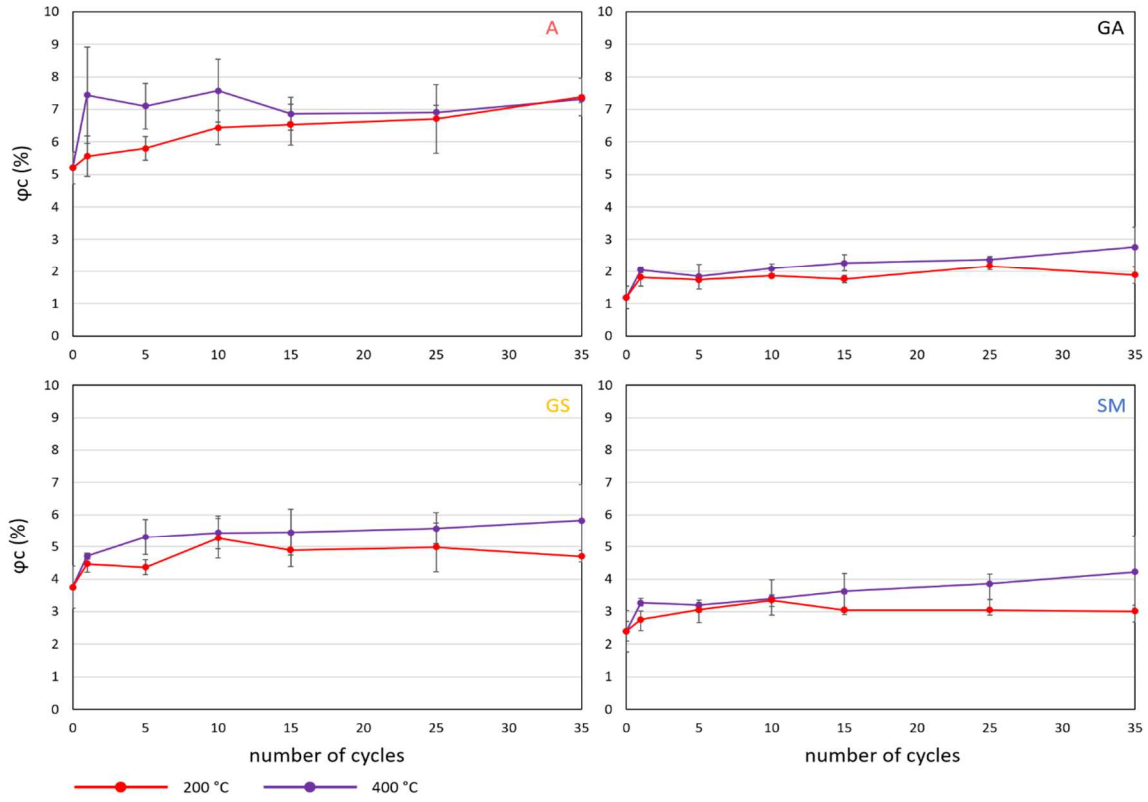

Fig. 7: Relationship between the number of thermal cycles and the connected porosity (φc) for the two quenching tests at 200 °C and 400 °C.

For each granite, the porosity showed an increasing trend with the quenching cycles, more remarkable after the first cycle, and greater when heated at 400 °C than at 200 °C. This increase was not monotonous for all granites. Indeed, φc decreased slightly for A from the first to the fifth cycle at 400 °C for example.

For A, the cycles at 200 °C revealed that the φc increased continuously with the number of cycles, with a change of 40% at the end of the test. At 400 °C, the φc did not show any further increase after the first cycle, with an abrupt increase of also around 40%.

For GA, at 200 °C the φc increased after cycle 1 and 25, with a variation of 60% at the end of the test. At 400 °C, after an abrupt increase during the first cycle, φc grew continuously until the end of the test with a change of 130%.

For GS and SM, the curves of the cycles at 200 °C indicated 2 slopes, a first until cycle 10 with continuous increase and a second from cycle 10 to 35, which showed a stabilisation, with a final variation of 25% at the end of the test. The curves at 400 °C of these 2 granites showed as for the rest of the rocks, an abrupt increase after the first cycle and a softer augmentation through the cycles, with a final increase of 55 and 75% for GS and SM respectively.

4.2. Capillary coefficient

The capillary absorption curves lasted over 72 hours, where the capillary coefficient (C) was obtained after the first linear part of the curve. The rise of the capillary fringe was complete for A, GS, and SM. For the GA granite, the water weight gain curve showed several breaks in slope and the capillary fringe did not reach the top of the sample. This incomplete rise reflected the low porosity values as well as the poor interconnection between the multiple families of pores and cracks. Figure 8 represents the evolution of the coefficient C of each granite during the two quenching tests.

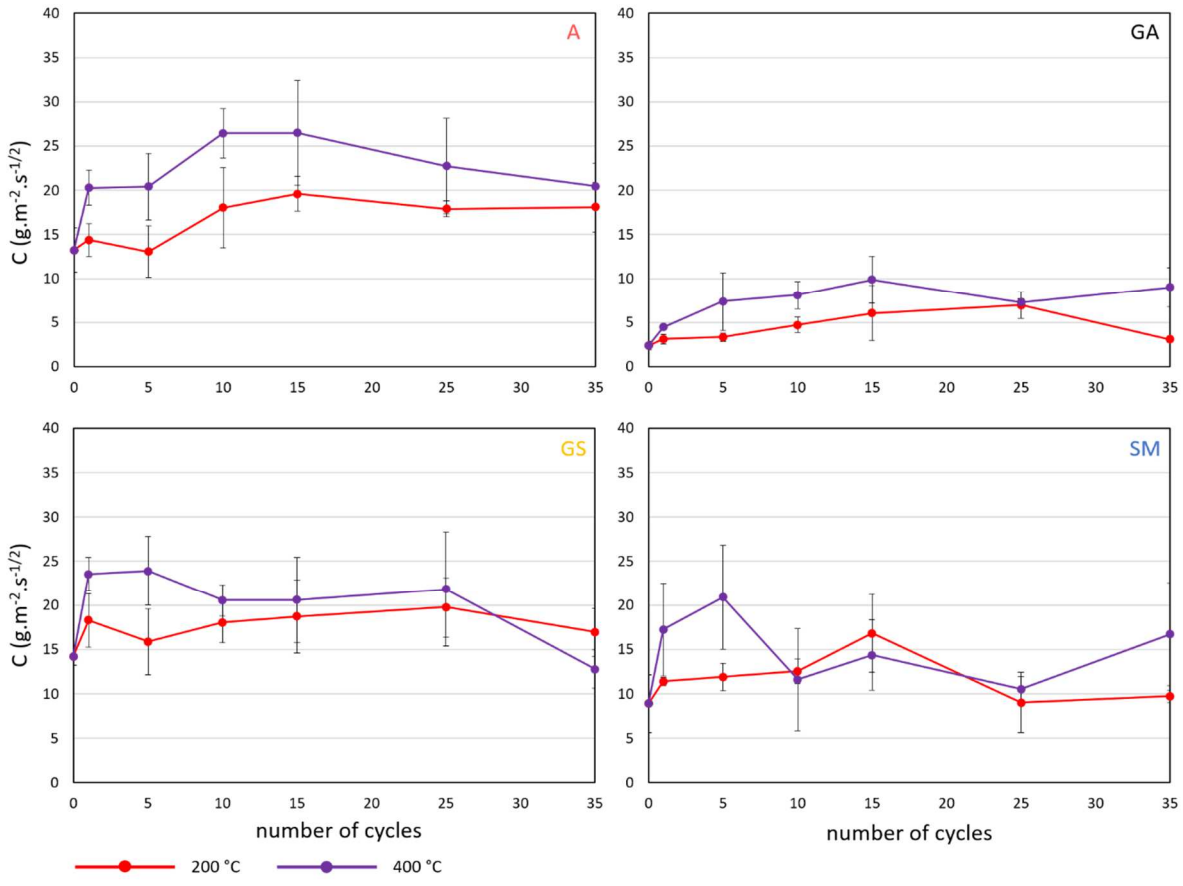

Fig. 8: Relationship between the number of thermal cycles and the capillary coefficient (C) for the two quenching tests at 200 °C and 400 °C.

For both quenching tests, capillary water absorption increased from the first cycle for all granites. In general, the increase was greater for rocks heated at 400 °C.

For A, at cycle 15, the coefficient C reached its highest value for rocks preheated at 200 °C with an increase of about 50%, and at cycle 10 for rocks preheated at 400 °C with an increase of about 100%. It only took one cycle of the preheated rock at 400 °C to reach a rise of 50%. From cycle 15, the coefficient C decreased for the two quenching tests and ended at cycle 35 with a final increase of 35% for the tests at 200 °C and of 55% for the tests at 400 °C.

For GA, although the general increase was significant for both quenching tests, the progression was greater on rocks preheated at 400 °C. The C coefficient of rocks preheated at 200 °C increased by 200% in a linear trend until cycle 25. This increase was comparable to the increase observed during cycle 5 of rocks preheated at 400 °C. From cycle 15, the coefficient C of rocks preheated at 400 °C stabilised after an increase of about 310%.

For GS, the capillary water absorption showed an irregular progression for the two quenching tests after an abrupt increase after cycle 1. The coefficient C increased to a maximum of 40% at cycle 25 for the 200 °C tests and 70% at cycle 5 for the 400 °C tests.

For SM, the rocks preheated at 200 °C, the coefficient C increases by 80% after cycle 15. The coefficient remained stable from cycle 25. Rocks preheated at 400 °C increased significantly by 130% after cycle 5.

4.3. P- and S-waves velocities and dynamic elastic moduli

Figure 9 shows the variations of the average of P-waves propagation velocities (Vp) and the attenuation coefficient (A) with the number of cycles. Each point corresponds to the average of the 18 samples measured from the initial state to cycle 35.

The granites preheated at 200 °C showed initially a gradual decrease in Vp with the number of cycles. A, GS, and SM exhibited a later stabilisation or even a slight recovery. Granites preheated at 400 °C showed a significant decrease in Vp after the first cycle, *i.e.* by approximately 26%, 15%, 23%, and 22% for A, GA, GS, and SM, respectively. Following this phase, the variations were smaller. The average rate of Vp decreased at cycle 35 by 34%, 25%, 23%, 27% for A, GA, GS, and SM, respectively.

For A, Vp gradually decreased by about 10% until cycle 14 at 200 °C, then remains stable. The coefficient A remained close to the initial value from the beginning at 200 °C. For 400 °C, Vp showed an overall decreasing trend with increasing cycles. The coefficient A decreased by about 40% after cycle 14 and then increased again.

For GA, Vp values did not show a significant variation, whereas coefficient A showed significant variation. The first cycles were marked by an increase followed by a decrease of about 60% after cycle 14 at 200 °C. The coefficient A increased again to reach the attenuation values of the initial wave. For 400 °C, Vp and the coefficient A decreased linearly up to cycle 35.

For GS, Vp decreased by approximately 10% until cycle 18 then gradually increased to reach the initial mean value again at cycle 33 at 200 °C. The coefficient A showed a similar trend with a decrease of approximately 50% after cycle 16, followed by an increase at 200 °C. For 400 °C, GS was the only one among the granites to have these Vp values which increased after the large falling after the first thermal shock cycles. The coefficient A also gradually increased after a decrease of about 40% after the first cycle.

For SM, a decrease of Vp of about 10% was observed after cycle 10, then a stable recovery to -7% of the initial value at 200 °C. After a balancing phase during the first 10 cycles, the coefficient A decreased by about 60% after cycle 13, then hovered around -40%. It is also noted that the values between samples had a high variability. For 400 °C, after a decrease at the first cycle, Vp remained between -20 and -30%. The coefficient A decreased by approximately 60 % at cycle 17, then increased slightly.

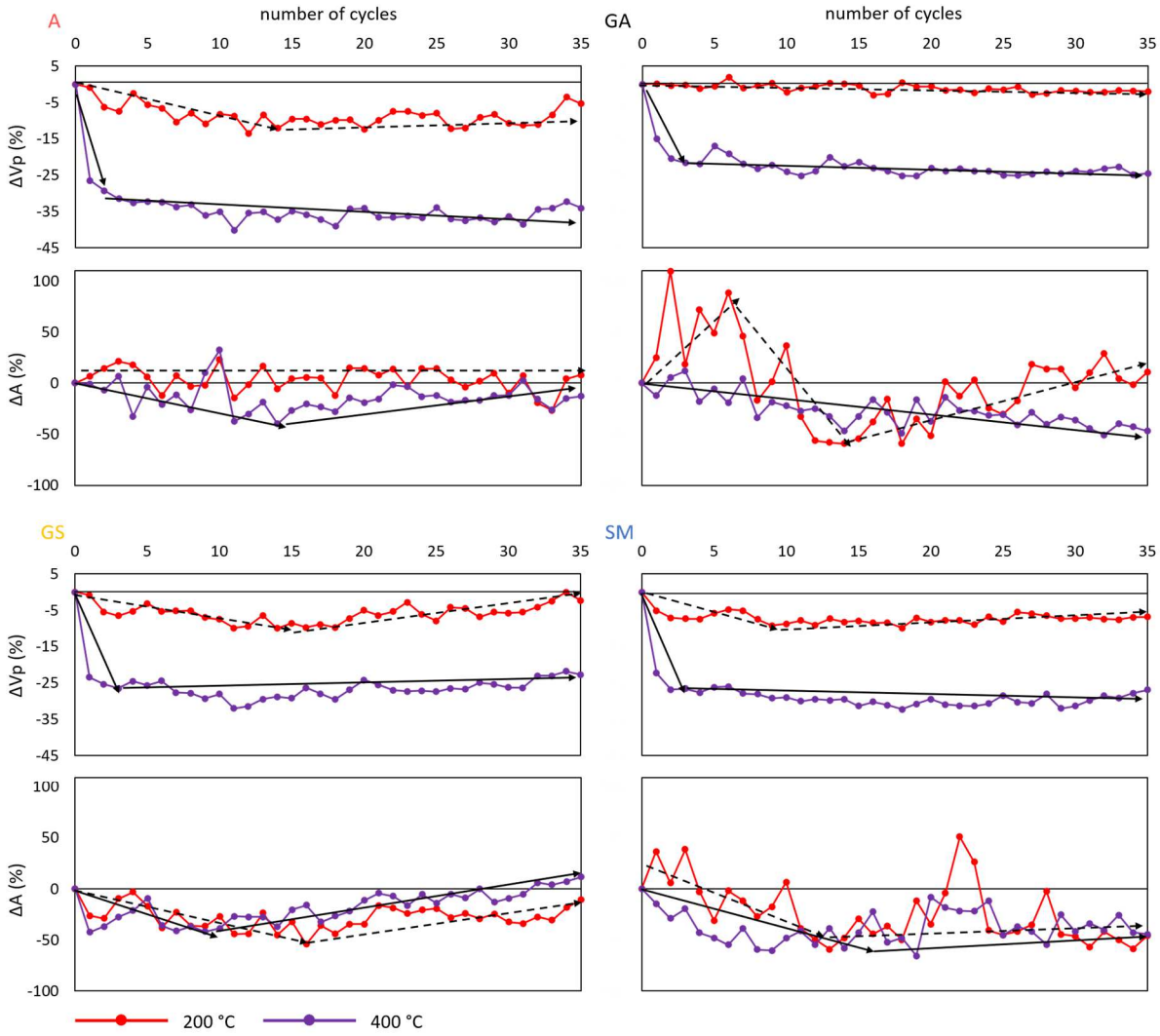

Fig. 9: Relationship between the number of thermal cycles and the percentage change in the P-waves velocity (Vp) and the amplitude coefficient (A) with the initial state. Solid and dashed black lines represent the trend for 200 °C and 400 °C, respectively.

The changes of the elastic modulus (E) of granites after heating (200 °C and 400 °C) and treatment with water are shown in Figure 10.

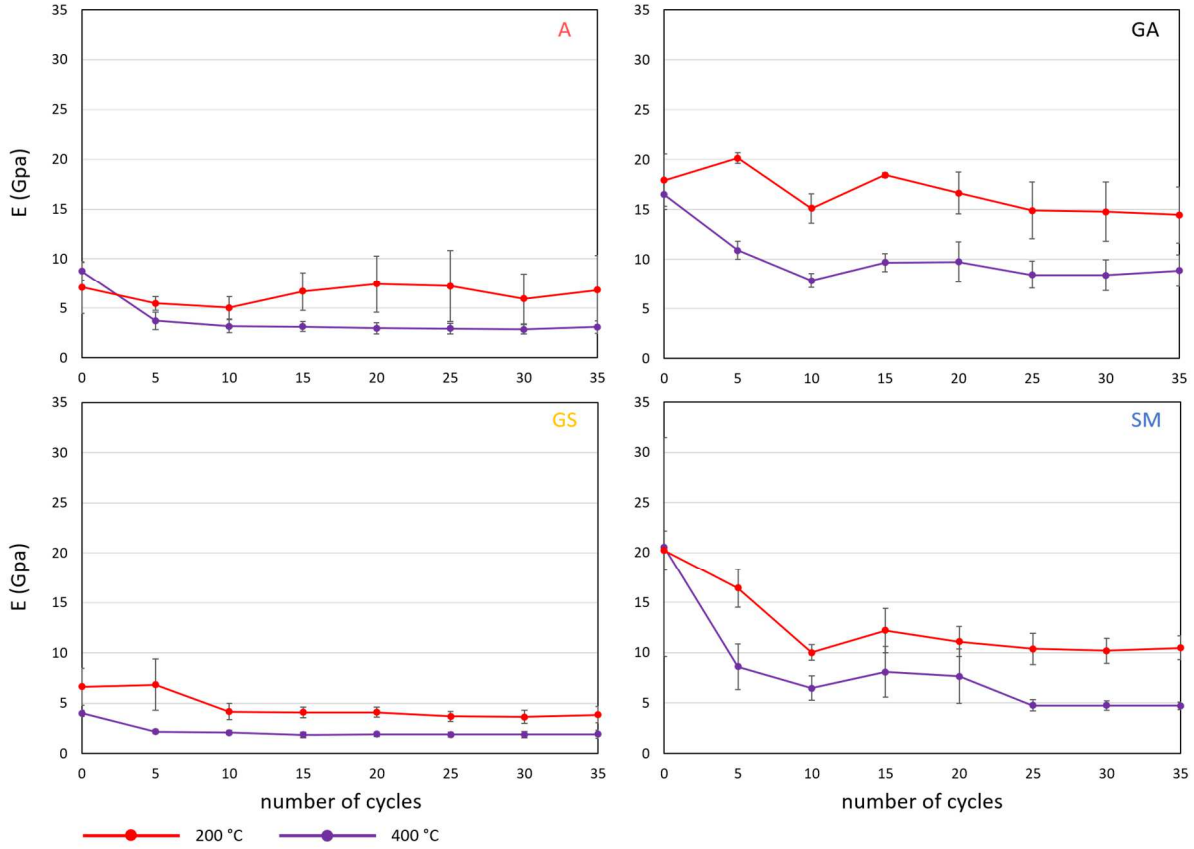

Fig. 10: Relationship between the number of thermal cycles and the Young's Modulus (E) for the two quenching tests.

For A, E decreased by approximately 20% from the first 5 cycles at 200 °C. Then, A remained stable around its initial value. For 400 °C, the values of E decreased significantly after 5 cycles, *i.e.* by about 60%, and then remained stable.

For GA, E showed an increase of 10% at cycle 5 then a decrease of 20% after cycle 35 at 200 °C. For 400 °C, the values of E decreased by 35% and 45% after 5 and 35 thermal treatments, respectively.

For GS, E remained stable after a 40% decrease after cycle 10 at 200 °C. For 400 °C, the values of E decreased by 45% and 50% at 400 °C after 5 and 35 thermal treatments, respectively.

For SM, E decreased by approximately 20% from the first 5 cycles at 200 °C and reached a decrease of 50% after cycle 35. For 400 °C, the values of E decreased by 60% and 80% at 400 °C after 5 and 35 thermal treatment, respectively.

4.4. Nuclear Magnetic Resonance relaxometry

We compared quantitatively the microstructure evolution of the studied granites using the transverse relaxation time, T2 (Fig. 11).

The quenching test at 200 °C did not show any variation during the first cycle, although at the end of the test A and SM increased their T2 values and showed a slightly greater amplitude. GA showed a slight decrease and GS shifted and reduced notably its signal (tighter cracks).

During the first cycle at 400 °C, A and SM evolve to similar values. GA kept a low signal amplitude before and after quenching and GS slightly decreased its amplitude. At the end of the test, A and SM slightly decreased their amplitudes but increased their T2 values. GA and GS showed little change from their initial state.

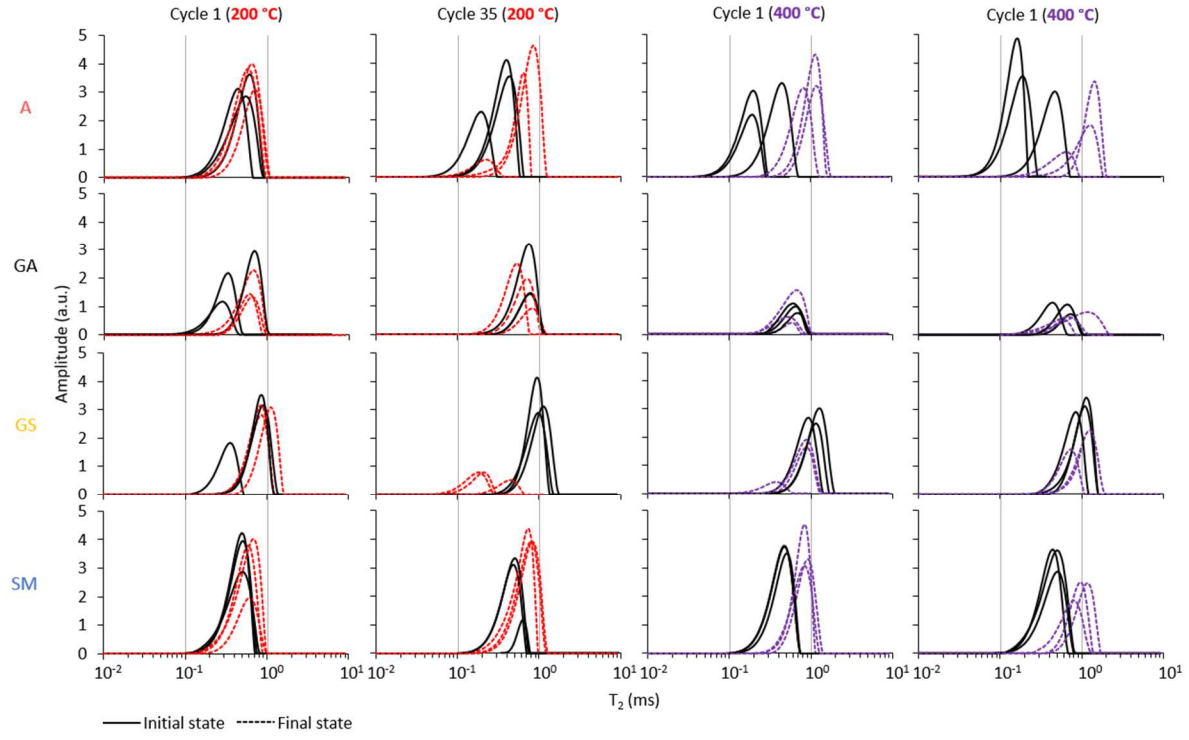

Fig. 11: Evolution of the transverse relaxation time (T2) distribution curves after 1 and 35 cycles. The initial and final state corresponding to the same samples.

In summary, A and SM showed similar behaviour to quenching with a slight increasing evolution of the geometric mean of this T2 distribution at 200 °C and a significant evolution from the first's cycles at 400 °C (Fig. 12). The general trend of GA does not show a clear change, and a slight decrease was still noted during cycles at 200 °C. Quenching at 200 °C on GS showed little change until cycle 15 and then decreased. Cycles at 400 °C showed an increasing phase up to cycle 5, and after stabilisation up to cycle 25, T2 values decreased.

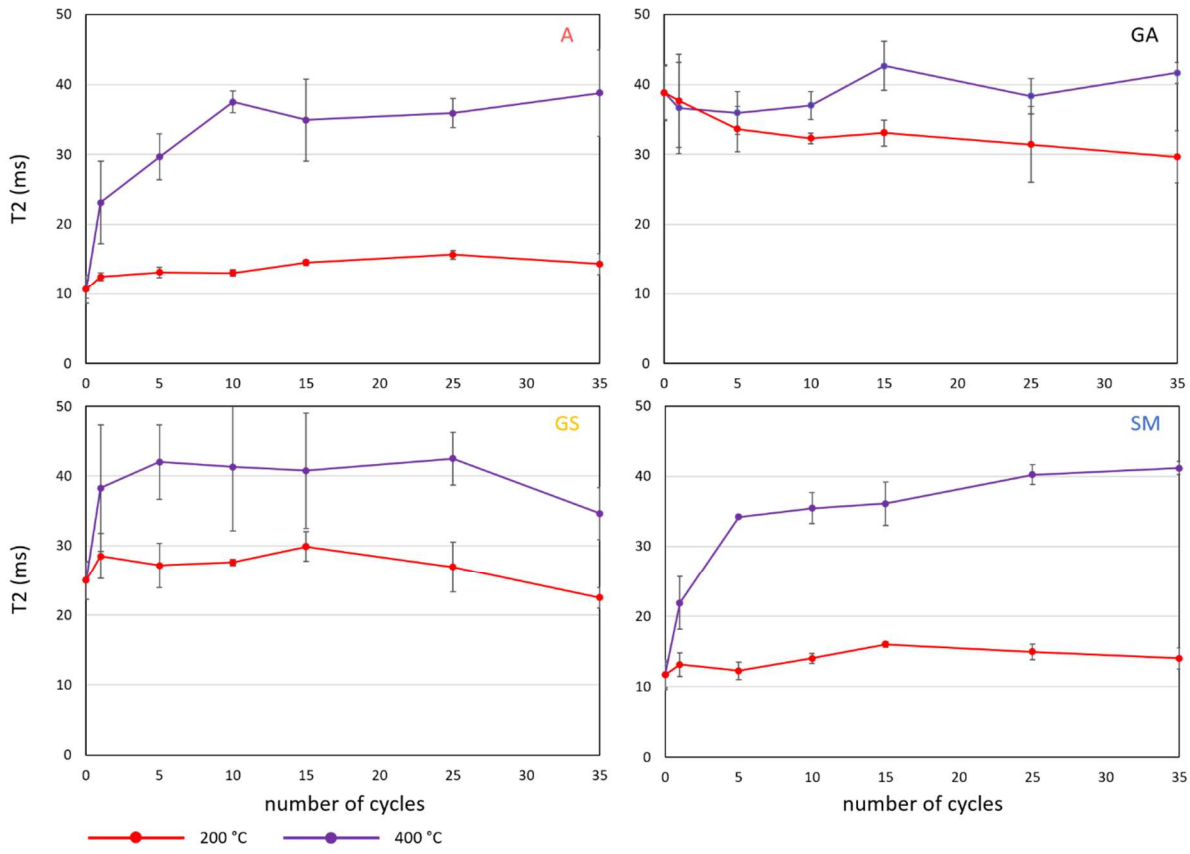

Fig. 12: Relationship between the number of thermal cycles and the transverse relaxation time (T2) for the two quenching tests.

4.5. Microstructural analysis with X-ray CT

GA and SM were assessed before and after 35 quenching cycles at 400 °C because their thermal sensitivity (Vazquez et al., 2018) and also since their porosity and Vp values come closest to granites widely studied and subjected to high temperature treatments (Vp greater than 3000 $m.s^{-1}$ and a low porosity of close to 1% (W. Zhang et al., 2018). To stablish the microcrack distribution of the studied rocks, three X-ray CT images of cross-sections in the x - y planes along the z height were taken before and after the test at 400°C, and they are shown in Figure 13. They exhibited significant microcracking at a resolution of 6 µm.

For GA, the initial state revealed mainly intra and intergranular microcracks in feldspars that sometimes are prolongated to quartz. After quenching cycles, the development of intergranular

514 microcracks along the quartz-feldspar crystal boundaries were detected. Some of these cracks
515 extended and formed intragranular cracks mainly in feldspars although also visible in quartz. As
516 observed by Isaka et al. (2019), microcracks in granites preheated up at 400 °C seem to stop their
517 progression when they encounter a crystal of biotite since the energy follow the path of the mica
518 boundary. Indeed, very few microcracks were observed inside the biotite. Some showed their
519 cleavage to open up after treatment (Fig. 13).
520 For SM, the fresh rock revealed that the initial microcraking was more notable than in GA granite,
521 with mainly long intragranular cracks that can be transformed into transgranular always through
522 feldspars, and also a network of and short cracks as a result of feldspar alteration. After quenching
523 test, the most remarkable change was the widening of pre-existent microcracks that prolonged as
524 intragranular microcracks and that predominated over the creation of new ones. The mica was not
525 attained by severe microcracking since the energy was absorbed and dissipated by their grain
526 boundaries as in GA.

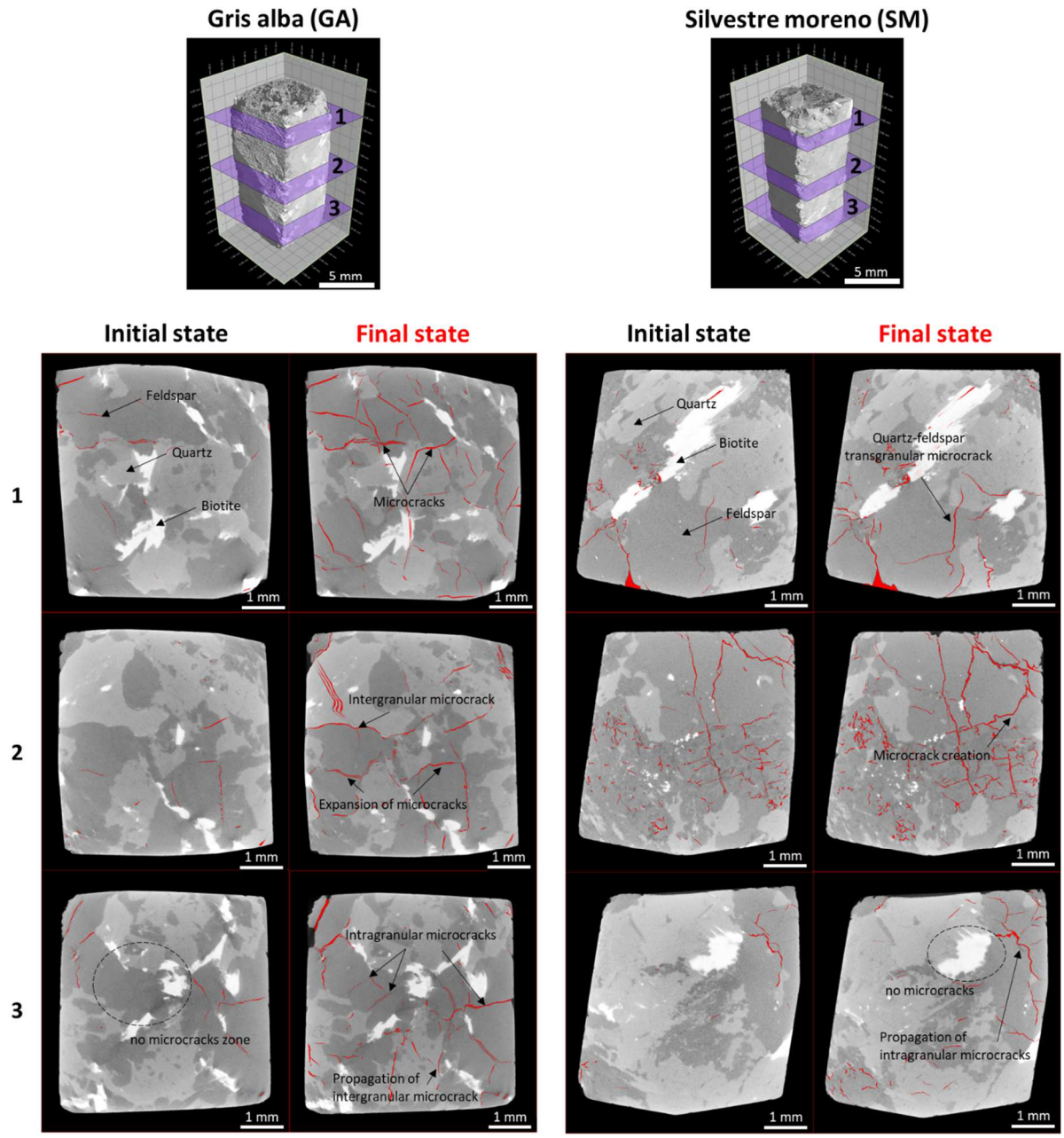

Fig. 13: Horizontal X-ray CT slides of GA and SM initial and final state (cycle 35) for three different elevations. The pores and cracks are presented in red color.

From the volume analyse of the X-ray CT data, a quantification of the microcrack variation can be obtained (Fig. 14). In general, the volume rendering of the porous networks showed that microcracks development were distributed evenly throughout the sample, before and after the tests so that the whole sample was affected by the quenching process. The porosity after treatment was 3.5 times greater for GA and 1.5 times for SM. The evolution in the degree of microcracking in the two granites increased the coefficient of variation (CV). At the initial state, this coefficient CV was

80% for both GA and SM and it increased to 85% and 108%, respectively after 35 quenching cycles at 400 °C.

In detail, image processing allowed the cracks to be detected and segmented. The parameters of the porous network (pore volume, pore number and diameter) were quantified and they are shown in Figure 14.

For GA, a notable increase (325%) of the pore volume was observed after quenching from 1121 to 4766 μm^3 meanwhile the number of pores decreased by 13%. The quantification of the pore volume as a function of their diameter, represented in Figure 14b, showed the formation of large pores (greater than 800 µm) during the final state of quenching. The histogram (Fig. 14c) showed the pore size distribution of GA before and after quenching. The frenquency of pores increased for all pore class except the smallest between 6-10 µm.

SM showed a smaller increase in pore volume (133%), with an average volume rising from 7175 to 16736 μm^3. However, the number of pores was reduced more significantly with a value of 35% (Fig. 14 b'). The histogram (Fig. 14c') evidence that pore diameters ranging from 6 to 15 µm predominate in the sample. After heat treatment, the number of pores or cracks with a diameter greater than 10 µm increased.

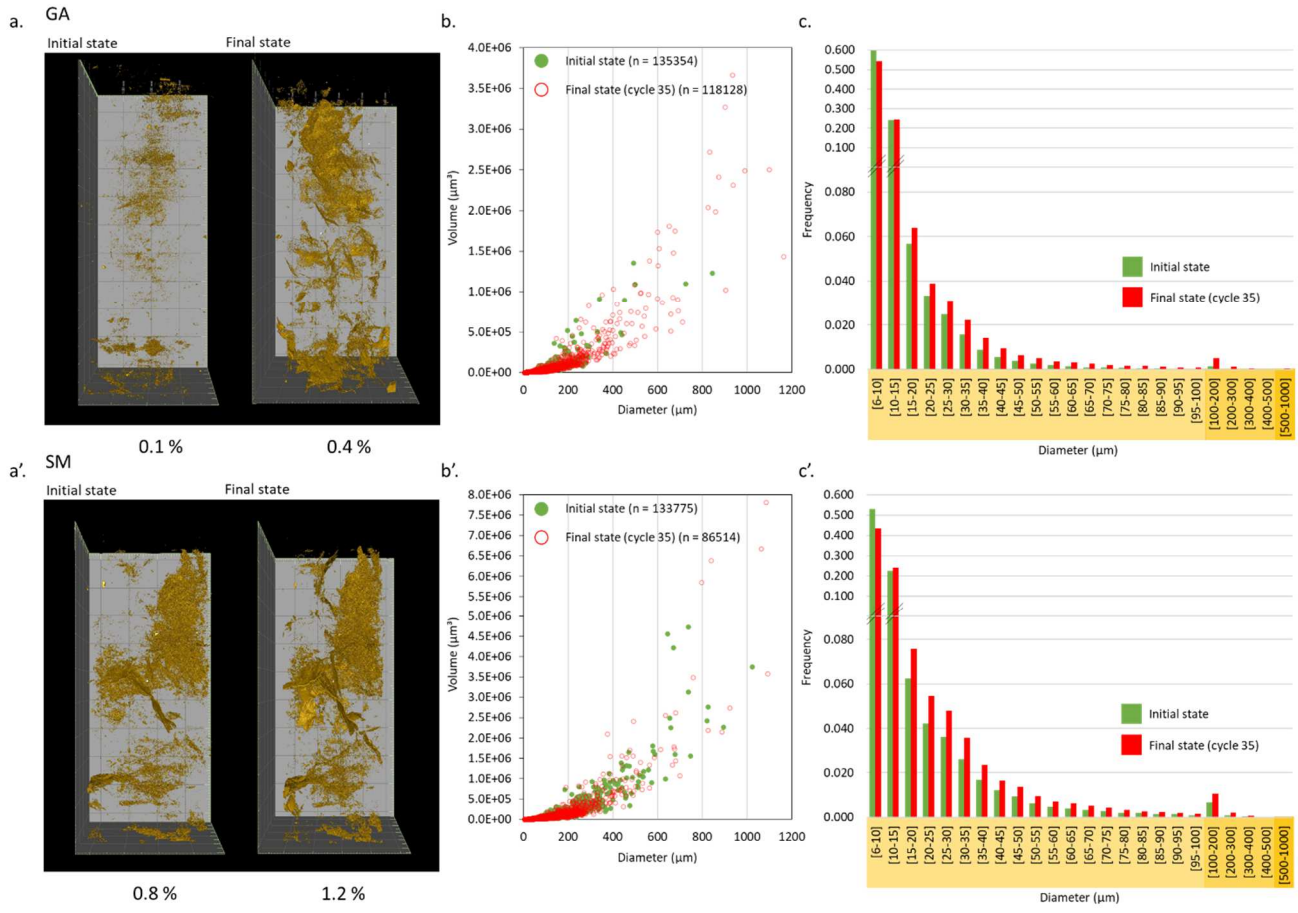

Fig. 14: Qualitative and quantitative data extracted from X-ray CT measurements before and after the quenching test (cycle 35). a-a'. Reconstruction of the 3D porous network. b-b'. Relationship between volume and diameter of pores. c-c'. Pore size-frequency distribution.

4.6. Mineral composition determined using XRF and chemical analysis of fluids

The granites in this study were mainly composed of quartz, K-feldspar, plagioclase, and micas. Table 3 shows the initial chemical composition of the granite samples determined by XRF, with slight variations between them.

Tab. 3: Chemical composition of the major elements expressed in percent.

	Na_2O	MgO	Al_2O_3	SiO_2	K_2O	CaO	Fe_2O_3
A	2.50	0.50	13.85	74.09	4.97	1.12	1.26
GA	3.42	0.70	14.38	71.26	5.52	1.54	1.58
GS	2.99	0.34	13.88	74.26	5.21	0.79	1.49
SM	3.29	0.46	14.43	73.35	5.92	0.52	1.42

Mineralogical and chemical alteration processes were carried out thanks to the ability of water to access the rock matrix via micro-fractures (Wogelius et al., 2020). This process then allows to mobilise part of the natural radionuclides and other trace elements from the primary minerals of the rock matrix as they are degraded. Figure 15 showed the cumulative concentration of dissolved elements as a function of the cycles on the water used for cooling.

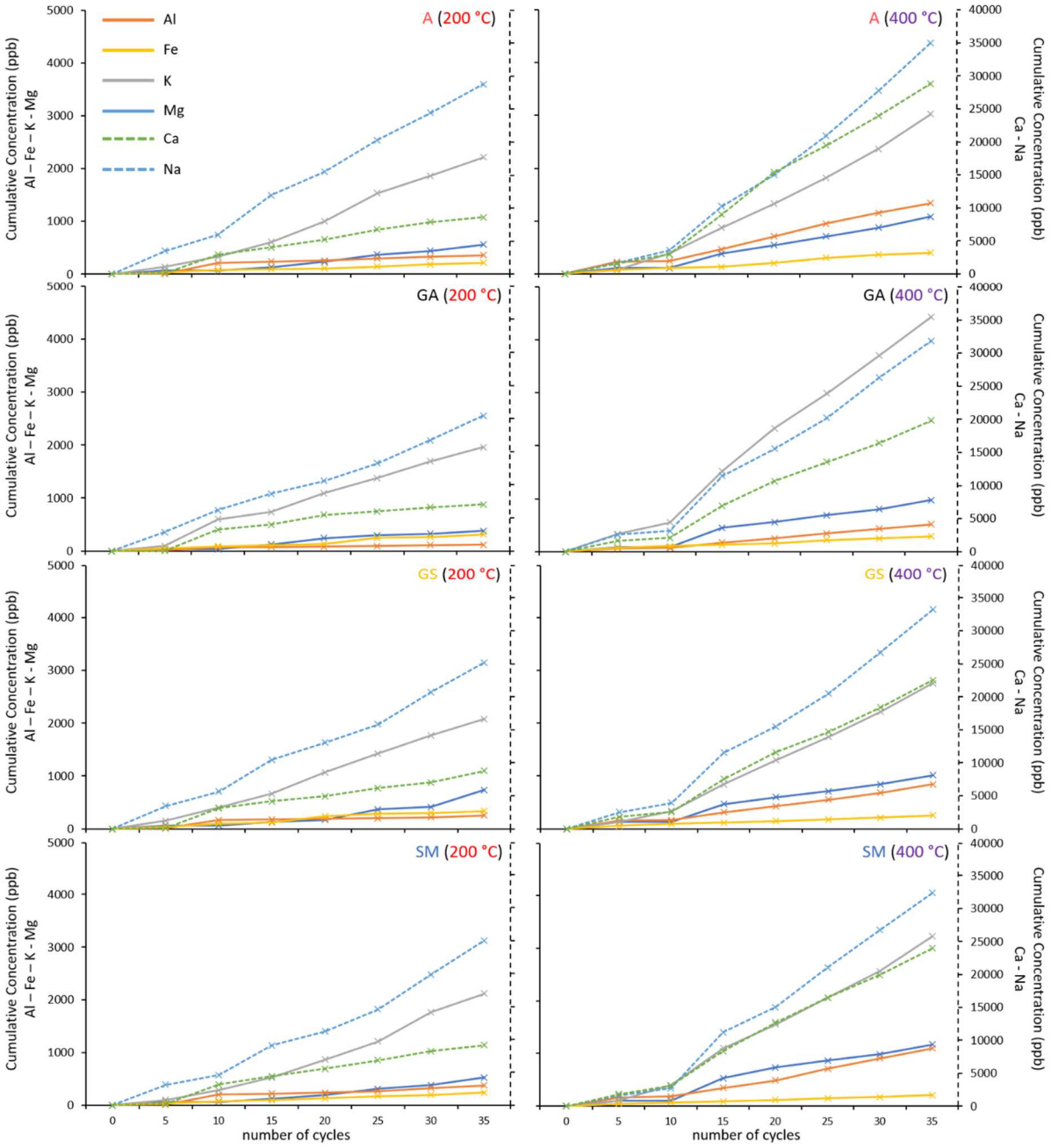

Fig. 15: Cumulative curves of the concentration (ppb) in Al, Fe, K, Mg, Ca, and Na in the solutions as a function of the number of cycles for the two quenching tests.

ICP-MS analysis showed an increase in the release of minerals in the liquid phase during cycles, more intense at 400 °C. In cycles at 200 °C, all the elements were dissolved with an almost linear trend. Tests at 400 °C showed an inflexion point after 10 cycles, from which the dissolution rate became faster and at the end of the experiment (cycle 35) the dissolution was greater than for the 200 °C tests.

5. Discussion

Figure 16 relates the four main parameters (initial porosity φc, capillary coefficient C, maximum signal amplitude of ultrasonic waves Amp, P-wave velocity V_P and Young's modulus E) used to judge the initial alteration of the granites in this study. The main observations are described below:

The unaltered granite (Gris Alba, GA) had the greatest value of ultrasonic wave amplitude, which resulted in a weakly attenuated ultrasonic signal compared to A, GS, and SM. Among all the granites, the unaltered granite exhibited the highest T2 values. This result was not apparently consistent with the porosity values, but the relaxation rate can be increased depending on the concentration and the mineralogical form of iron oxides for example (Keating and Knight, 2006) and the clay content can also reduce the pore size of weathered granite.

The slightly weathered granite (Silvestre Moreno, SM) had the highest Young's modulus values, which indicated high rigidity and a low amount of damage within the structure.

The moderately weathered granite (Golden Ski, GS) had the lowest mechanical properties and the highest capillary coefficient values. The capillary absorption coefficient was directly linked to the pore size and quantified the flow mechanisms influenced by the pore structure and the interconnectivity of the pores (Benavente et al., 2002; Cai and Yu, 2011; Çelik and Kaçmaz, 2016). The moderately weathered granite, the transverse relaxation time T2 values in NMR were the highest among the initially weathered granites, indicating a large pore size allowing good migration of the fluid.

The highly weathered granite (Albero, A) presented the largest pore volume. The ultrasonic wave attenuation of this granite was the highest, due to the individual microcracks distributed in the sample (Benavente et al., 2020). The low Vp values in the moderately and highly weathered granite were indicative of the high initial microcrack density.

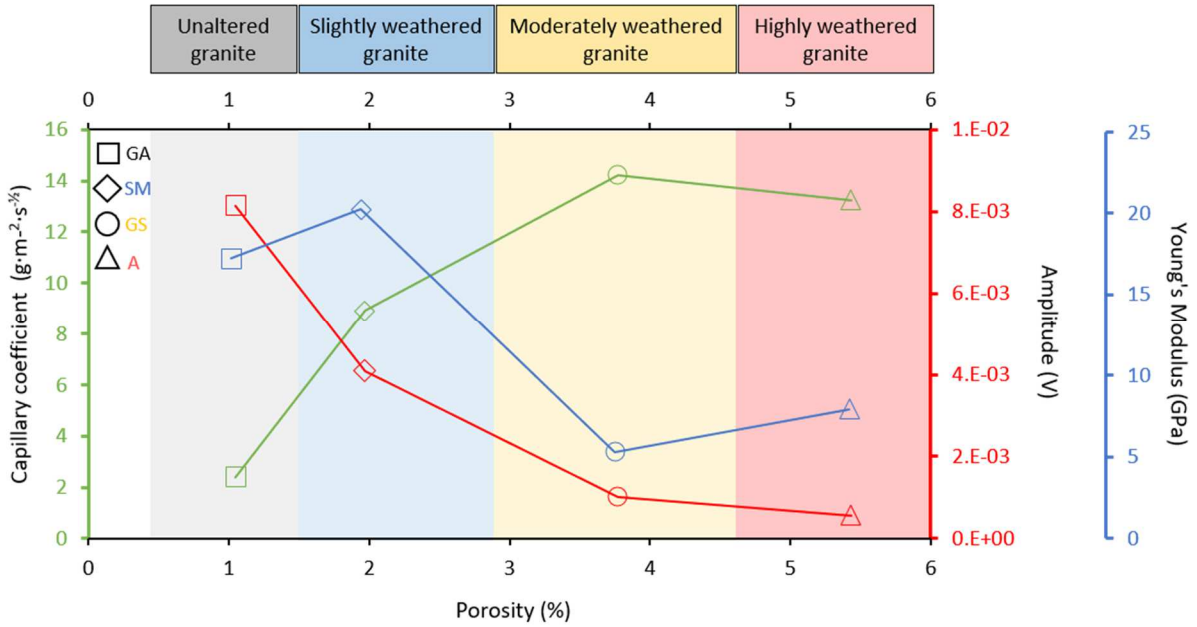

Fig. 16: Relationship between the initial porosity of the granites and their capillary coefficient, maximum amplitude of the P-waves, and Young modulus.

5.1. Effects of repeated quenching on damage

In geothermal engineering, extracting heat from deep rocks by injecting water into the well brings about a quenching process. The repetition of this operation can induce instability in the drilling at the expense of its profitability. The degree of cracking depends mainly on temperature and pressure stress, mineralogical composition, and particle size distribution (Freire-Lista et al., 2016). Due to this brutal thermal gradient during quenching, a thermal expansion occurs in the structure resulting in a thermal shock cracking (Kumari et al., 2018).

Quenching generally leads to tensile stress tangential to the surface of the rock. After a thermal shock, the damage near the surface is often greater than inside the sample (Fan et al., 2020). The damage to the surface of the granite sample may become more concentrated, resulting in nucleation of surface microcracks (Yu et al., 2020). The theoretical relationship exposed by Kim et al. (2014) allows estimating the maximum tangential tensile stress generated at the surface of the granites studied (σt max) (Tab. 4).

$$\sigma t = \frac{E \alpha \Delta T}{1 - \nu} \quad (6)$$

where E is the average Young's modulus of samples fast cooled from 200 or 400 °C respectively, α is the thermal expansion coefficient, ΔT is the difference temperature, and ν is the Poisson's ratio. The calculations for the studied granites used the thermal expansion coefficients from Vazquez et al. (2011, 2015).

Tab. 4: Maximum tangential tensile stress generated (σt max) at the surface of the granites during the quenching after the two preheating treatments and experimental tensile strength test (Vazquez et al., 2018[1]).

	Mechanical properties: Tensile strength (MPa)[1]	σt max (MPa)	
	25 °C	200 °C	400 °C
Unaltered granite (GA)	9.3	41.9	50.5
Slightly weathered granite (SM)	4.9	43.3	48.9
Moderately weathered granite (GS)	4.0	15.8	12.2
Highly weathered granite (A)	4.4	16.3	22.1

The maximum tensile stresses that could be generated at the rock surface during quenching are much greater than the tensile strength of these granites measured experimentally at room temperature (Tab. 4, Vazquez et al., 2018). Samples preheated at 400 °C and then immersed in cold water (25 °C) showed a maximum tensile stress greater than at 200 °C. For example, the maximum tensile stress of about 50 MPa could be generated at the surface of the unaltered granite. These values were sufficient to produce significant thermal cracking as observed by the measured properties and the images from X-ray CT (Fig. 13).

The stress propagation from the surface to the interior of the sample, was directly related to the preheating temperature and the number of cycles. For both test, there was a fatigue threshold, that was the number of cycles from which the damage affected similarly the whole sample and the measured values were maintained or varied only slightly due mainly to crack redistribution. During repeated heating cycles, rocks can exhibit a stress memory effect, or the so-called Kaiser effect (Kaiser, 1953) which indicates that in order to sustain damage, a material must be subjected to stresses greater than those it has already experienced. This characteristic can be observed in many EGS sites during forced fluid injection operations (Maurer et al., 2020) and also under heat stress in the laboratory in a wide variety of rock types (Lavrov, 2003). For example, Yong and Wang (1980) have shown that there may be a Kaiser effect on the Westerly Granite because during the heating process and at temperatures below the peak temperature of the previous cycle, very little acoustic emission occurred.

Figure 17 shows the parameter changes of quenching samples preheated at 200 °C and 400 °C with cycles. The damage variability was defined taking into account the initial standard deviation and the

extreme values of all the granites. For rocks preheated to 200°C, at least between ten and fifteen cycles of quenching were necessary to reach the stress threshold or Kaiser Effect, although certain properties and granites revealed a continuous progression of microcracking until the end of the test. Meanwhile for those rocks preheated to 400°C, some definitive variations were observed from the very first cycle. The inadequacy of the thermal expansion coefficients of the different minerals prompted the generation of microcracks, causing significant damage to the granites (Jin et al., 2019; Sousa et al., 2005; Wu et al., 2019).

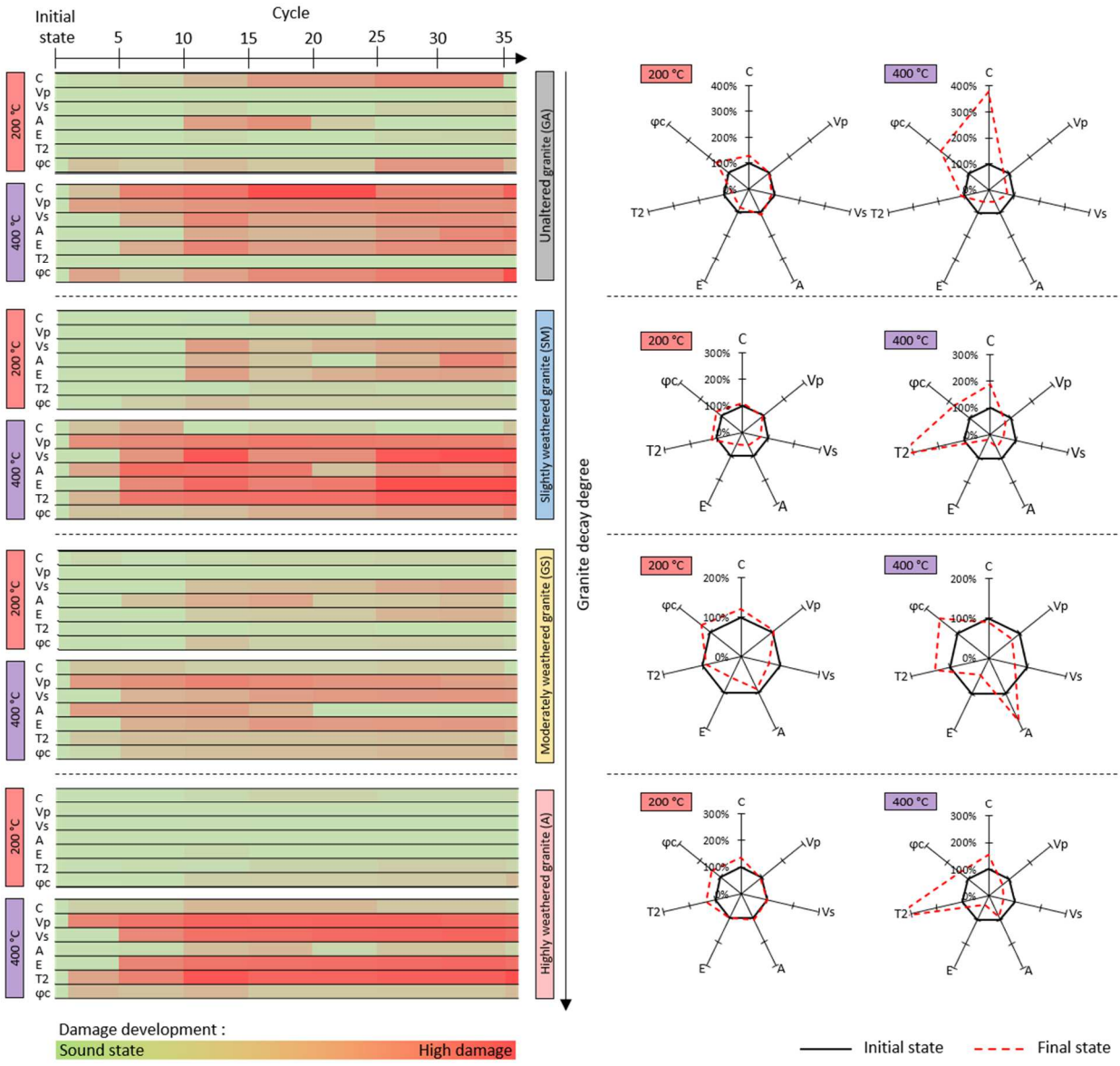

Fig. 17: Evolution of the parameters measured for the two quenching tests. C: capillary coefficient; Vp: P-wave propagation velocity; Vs: S-wave propagation velocity; A: Amplitude coefficient; E: Young's modulus; T2: Transverse relaxation time and φc: Connected porosity.

Figure 18 relates the microstructural changes with the petrophysical properties measured. Two kind of behaviours can be differenced in relation to the initial weathering.

662 The unaltered granite GA, showed at 200°C, a progressive degradation until the end of the test. The
663 main parameters affected were the porosity and the capillarity that indicated an increase in the
664 volume and connectivity of the pores. The low initial porosity may influence the slight variation
665 related to the mechanical parameters. At 400°C, the change of these two parameters was enhanced
666 and accompanied by a noticeable increase in the microcracking as indirectly measured by
667 ultrasounds. In agreement with Zhu et al. (2020), Vp showed an approximately 40% reduction at 400
668 °C after 30 quenching cycles with a significant decrease from the very first cycle. This behaviour
669 agreed with the microcracking development observed in the figure 13, where X-ray CT also revealed
670 a propagation mainly in intergranular cracks that enhanced connectivity (Fig 18).
671
672 The weathered granites showed a variation in microstructure due to crack propagation and opening,
673 although without improving connectivity. The development of microcracking detected by ultrasound
674 parameters and also observed by X-ray CT revealed a widening and propagation of transgranular
675 microcracks that were not forcedly connected between them. For the three granites and both
676 temperatures, 200°C and 400°C, connected porosity and capillary coefficient hardly changed. At 200
677 °C, noticeable changes were measured after 10 cycles, followed by stabilization. Albero, the most
678 weathered granite hardly showed any variation. At 400°C, a strong decrease in the dynamic and
679 elastic parameters related to strength were measured from cycle 1 to 5. The small microcrack
680 network observed in feldspars and the widening of long intragranular cracks may experiment
681 readjustments during the rest of the cycles although without improving connectivity (Fig 18).

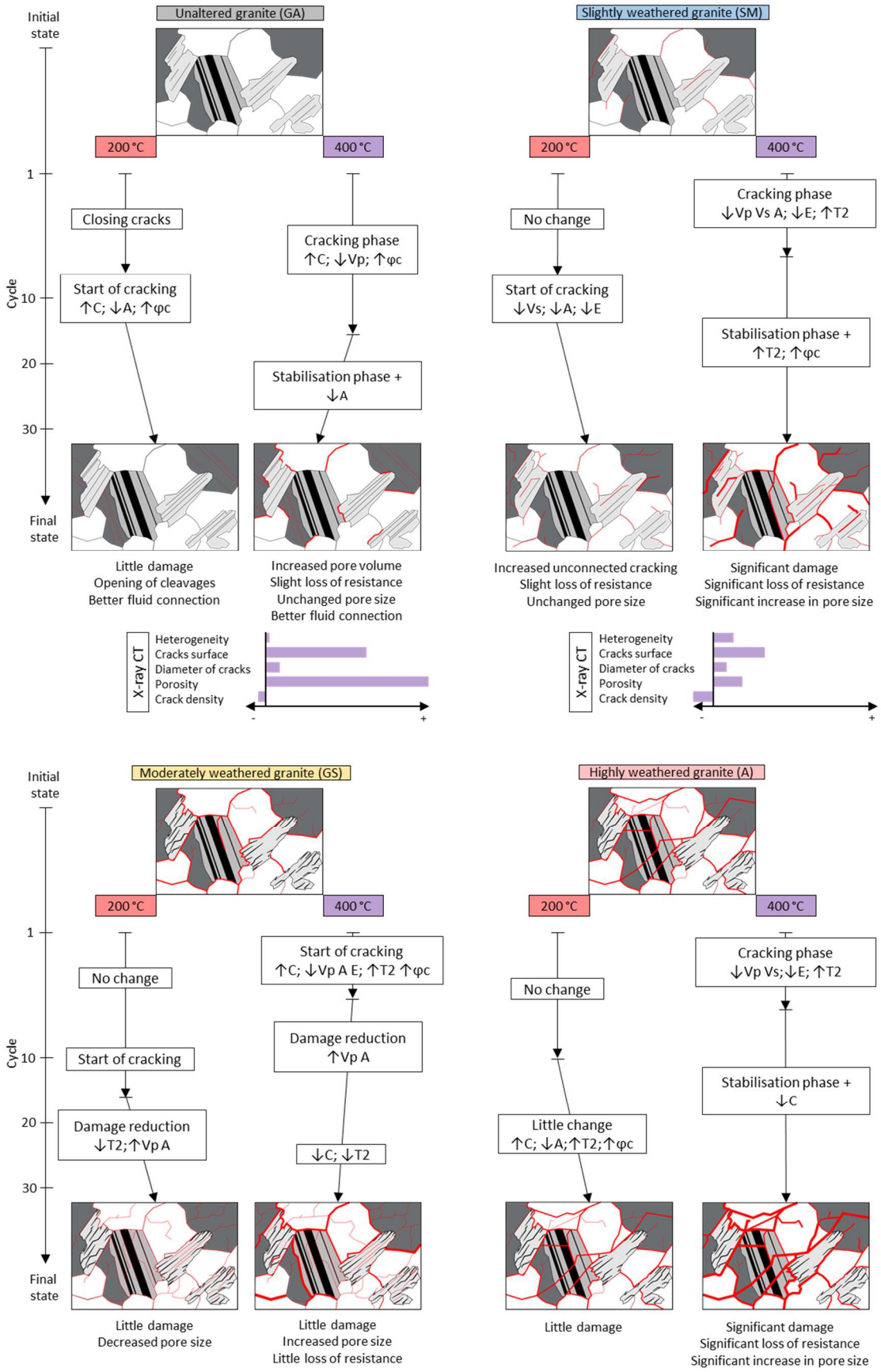

Fig. 18: Synthesis of microstructural observations of the granites after quenching from 200°C and 400°C. ↑: increase; ↓: decrease; C: capillary coefficient; Vp: P-wave propagation velocity; Vs: S-

wave propagation velocity; A: Amplitude coefficient; E: Young's modulus; T2: transverse relaxation time and φc: Connected porosity.

5.2. Damage evaluation and permeability

With increasing the crack density and increasing the number of cycles, cracks can penetrate more easily, which improves the permeability. On the other hand, the strong thermal gradient generated would tend to cause damage in the borehole.

Permeability is an important parameter that is generally used to describe the ability of the rock to allow the flow of fluids through its pores. The permeability (k) was estimated from the Schlumberger-Doll Research (SDR) equation (7), based on the Kozeny-Carmen equation, as indicated in the following equation (Kenyon et al., 1988; Straley et al., 1997):

$$k = b\varphi^{m}(T2_{LM})^{n} \quad (7)$$

Where φ is the porosity, $T2_{LM}$ is the mean log of the T2 distribution, and b, m, and n are empirically determined parameters. Each of the SDR parameters is expected to have a dependence on the lithology.

The porosity exponent m is associated with the Archie's formation resistivity factor (Chang et al., 1994). The exponent of the relaxation time n is associated with the grain size distribution (Dunn et al., 1999). For consolidated materials, m = 4 and n = 2 are the most commonly reported values (Knight et al., 2016; Ren et al., 2019). The constant b is considered to be dependent on the lithology and is related to the surface relaxivity ρ. It represents a practical calibration parameter to take into account these other properties independent of geological materials which are difficult to measure or quantify to obtain the best possible match for predicting permeability (Maurer and Knight, 2016). In petroleum applications, for m = 4 and n = 2, the standard value of b is 4 mD ms^{-2} = 3.95x 10^{-9} $m^2.s^{-2}$ (Kenyon et al., 1995). We set these parameters for this study.

As indicated in section 5.1, the quenching cycles induce significant damage on the granite.

The thermal damage which is related to Young's modulus was thanks to the damage factor D_E (T) (Guo et al., 2018; Sha et al., 2020; W. Zhang et al., 2018), indicated in the following equation:

$$D_E(T) = 1 - \frac{E_t}{E_0} \quad (8)$$

Where E_0 and E_T are the values of the modulus of elasticity at room temperature, and temperature T (200 °C-400 °C), respectively. The application of this calculation was carried out at the two treatment temperatures and as a function of the number of cycles.

Figure 19 represents the evolution of the permeability k and the damage factor D_E as a function of the number of cycles. For each cycle, the average value of three samples is given.

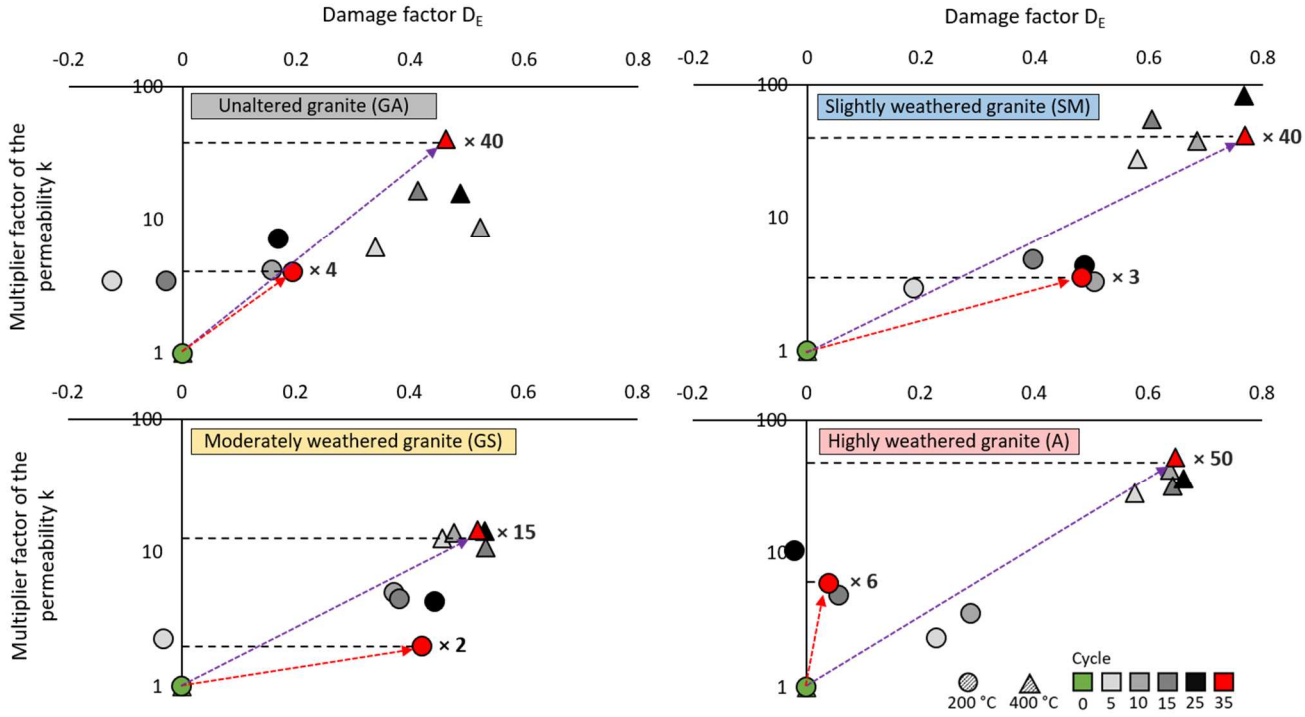

Figure 19: Evolution of the permeability k and the damage factor D_E as a function of the number of cycles. Samples preheated at 200 °C and 400 °C are represented by circles and triangles, respectively. The red and purple arrows represent the direction of the evolution of the 2 parameters. The base of arrows is positioned on the average value of 3 initial samples and having reached the average value of 3 samples of the final cycle.

Thermally induced fractures have improved the permeability of all the samples after 35 cycles at 400 °C. The critical temperature for which the permeability of granite significantly increases (Zhao et al., 2017) is set at 400 °C (Jin et al., 2019). Increasing crack density also leads to an increase in damage factor (Feng et al., 2020; Guo et al., 2018; Sha et al., 2020). The changes of the Young's modulus (E) were smaller during the quenching test at 200 °C than at 400 °C. At the end of the 35 cycles of quenching of the samples at 400 °C, E had decreased by 2.3, 1.6, 2.0, and 2.6 times that values compared to the thermal cycling performed at 200 °C for A, GA, GS, and SM, respectively. If rocks heated at 200 °C still showed variability between cycles, on the other hand at 400 °C, the main changes were made during the first cycles.

At the end of the quenching tests, the permeability of the unaltered and slightly weathered granite was improved by a factor of approximately 5 at 200 °C and by a factor of 40 at 400 °C. At the same processing temperature, quenching showed more damage on the slightly weathered granite which could be due to its larger grain size (Shao et al., 2014).

742 The permeability of the moderately weathered granite was less affected by the quenching.
743 Quenching cycles closed induced fractures after the first cycles following volumetric expansion
744 (Barton, 2007), reducing hydraulic connections.
745 The 50-fold increase in permeability occurred after the first 5 thermal cycles for highly weathered
746 granite (A) and was accompanied by a significant damage unlike quenching at 200 °C. This suggests
747 that microcracks dominated the flow pathways through the sample.

748 ## 5.3. Chemical analysis of fluids

749 The experimental fluids showed chemical element concentrations indicating signs of alteration of
750 minerals present in the granite. The main reactive minerals were alkaline feldspars and clays. The
751 increase of elements K and Al in the resulting water could be produced by the gradual alteration of
752 alkali feldspar. In general, these 2 main elements resulting from water-granite rock interactions
753 come mainly from the alteration of clays. They would be introduced into the fluid phase by the
754 degradation of the surface of clay minerals such as smectite, illite, or kaolinite. K, Mg, Mn, Ti in the
755 fluid came from biotite during the opening of the mica cleavages with temperature (Vazquez et al.,
756 2015).
757 Ca can be found in the saturating fluid by the degradation and dissolution of plagioclases (Wogelius
758 et al., 2020). Indeed, calcite-mineralised, transgranular, and intra-granular microcracks were
759 particularly frequent in plagioclase crystals, which generally show exolution or zonation figures
760 during their crystallisation. The composition of the water showed a slight increase in Fe. This
761 enrichment may be due to iron degradation from biotite (Vazquez et al., 2016).
762 The K-feldspar-water interactions must lead to an increase in Al, Si, K, and Na in the fluid from 200 °C
763 (Drüppel et al., 2020). Based on the ICP data, the increase of the concentration of all the mentioned
764 elements with the number of cycles for the two quenching tests could be attributed to the
765 dissolution or mechanical deterioration of K-feldspar. It was noted that this dissolution kinetics was
766 greater for rocks preheated at 400 °C. Feldspar crystals observed on X-ray CT showed intergranular
767 and intragranular cracking.
768 The unaltered granite showed the highest K content during the final cycle at 400 °C. An evident
769 intragranular microcrack was observed in K-feldspar which can go as far as coalescing with other
770 intergranular microcracks (Fig. 13). However, this high content can be interpreted by the high
771 proportion of K-feldspar compared to other granites.
772 While the observed chemical alterations were independent of physical processes, minerals that
773 underwent more physical deterioration also suffered more chemical alteration.
774

5.4. Potential application of quenching in Enhanced Geothermal System (EGS) projects

Quenching of granite formations is closely linked to the implementation and the development of EGS projects. Stimulation of a rock reservoir by hydraulic fracturing from water at room temperature is often adopted to improve the porosity and permeability of the rock. The permeability obtained in this study was an estimate calculated from the NMR petrophysical data, used specifically as a comparison between four granites, while capillary imbibition testing was used as an estimator of rock degradation and conductivity index. It is inversely linked to the durability of stone (Benavente et al., 2004; Çelik and Kaçmaz, 2016; Fronteau, 2000; Sengun et al., 2014). Knowing the movement of water inside the rock is a simple way to assess the porosity of the rock (Fronteau et al., 2010). Benavente et al. (2015) show a strong relationship between the coefficient of water absorption by capillarity and water permeability.

The experimental results showed that whatever the granite tested, the effect of the thermal shock increased the permeability estimated by NMR and that the connectivity of the water by capillary imbibition could vary according to the type of granite.

In addition, the higher the temperature of the formation, the more the thermal stimulation will create cracks in the formation. The irreversible cracking stress was not always at 200 ° C to generate the Kaiser effect, as for the sound granite GA. As a Kaiser effect was observed during heating to 400 ° C and rapid cooling, it can be concluded that the improvement of the permeability around the geothermal wells would be effective from the first cycles, but renewing the thermal stimulation would not be more beneficial. Indeed, heating the rock in repeated cycles without inducing cracking could induce a closure of the pre-existing microcracks with the expansion of the rock matrix. Thermal stimulation can be used to rapidly increase the permeability of rocks and thermal fatigue could potentially strengthen the rock mass or to remobilize the porous network.

The experimental data also showed that as the quenching progressed, fracturing increased which would lead to a decrease of the mechanical properties. Transcribed to the geothermal system, this observation means that if the thermal stress exceeds the equilibrium threshold of the surrounding deep rock system, zones of fragility could be created. The mechanisms involved during hydraulic stimulation could locally modify the stresses that could be at the origin of microseismicity, that may cause damage to local populations. Between June and July 2000, a hydraulic stimulation experiment took place at the EGS geothermal site in Soultz-sous-Forêts (Alsace, France) and more than 7,200 microseismic events were located in the range of magnitude –0.9 to 2.6 (Cuenot et al., 2008). In 2006, the geothermal energy project in Basel (Switzerland) was stopped due to a seismic event of magnitude greater than 2.0 which caused some damage to buildings. Therefore, during hydraulic fracturing, it is necessary to ensure that the quenching only reaches the area dedicated to fracturing.

809 It is therefore necessary to implement technologies such as thermal insulation of pipelines (Shen et
810 al., 2020).
811 In this study, we focused on the effect of thermal cycling on the petrophysical properties of granite
812 after quenching and hoped to contribute to the stability of boreholes when exploiting deep
813 geothermal energy. All the tests were performed in an unconfined condition. However, geothermal
814 reservoir rocks are subject to confinement pressure. Therefore, the behaviour of granite after
815 quenching under these conditions requires further studies.

816 6. Conclusion

817 The study of quenching damage is essential to understand the fracturing on the permeability of the
818 reservoir and therefore the life of a geothermal installation. In this work, the thermal shock
819 behaviour of four granites with different initial properties was followed. From the results of the
820 study, the following conclusions are drawn:
821 Strong correlations between the coefficient of capillarity, the P- S-wave propagation velocity,
822 Young's modulus, and the porosity have been established. The size of the cracks measured with the
823 NMR showed an increased with the number of cycles. Due to the different crystal structure of the 4
824 granites, the thermal stress limit threshold and the cracking morphology is different. If crack
825 openings or closings occurred in weathered granites during thermal shocks, the size of the
826 microcracks did not change in the sound granite but their density did. The change if the predicted
827 permeability was a direct consequence of the propagation of microcracks induced by the strong
828 gradient during quenching tests.
829 A single cycle of a thermal shock for rocks preheated at 400 °C prompted more damage than after 35
830 cycles at 200 °C. The propagation of pre-existing cracks was observed with X-ray CT and the
831 enlargement of the size of the cracks with NMR, especially for granites with the smallest initial T2
832 value (A and SM).
833 In the case of rapid quenching from 400 °C, intragranular microcracks within the K-feldspar
834 propagated throughout the low initial porosity granites (the unaltered GA and the slightly weathered
835 SM). For these less weathered granites, the expansion and contraction of the minerals lead to
836 greater damage inside the crystals. The increase of connectivity improves the permeability while the
837 more weathered granites experimented an increase of microcracking with less connectivity.
838 The chemical analysis of the fluids used for cooling served as clues of the mineralogical alteration
839 and allowed the alteration processes to be evaluated. The water-granite rock interaction showed the
840 dissolution of K-feldspar, plagioclase, and the degradation of clays, leading to an enrichment mainly
841 in K, Na, and Ca in solution.

Declaration of Competing Interest:

The authors report no declarations of interest.

Acknowledgments:

This work was carried out within the framework of the FLUTE Project. We would like to express our deep gratitude to our partners from the University of Reims Champagne-Ardenne (France), La Région Grand Est and Regional Government of Comunidad Valenciana (Spain) [grant number AICO/2020/175], for their kind scientific collaboration and participation in the development of this project.

Reference

Albissin, M.C., Sirieys, P., 1989. Thermal Deformability of Rocks: Relation to Rock Structure. Presented at the ISRM International Symposium, International Society for Rock Mechanics and Rock Engineering.

Alt-Epping, P., Diamond, L.W., Häring, M.O., Ladner, F., Meier, D.B., 2013. Prediction of water–rock interaction and porosity evolution in a granitoid-hosted enhanced geothermal system, using constraints from the 5km Basel-1 well. Applied Geochemistry 38, 121–133. https://doi.org/10.1016/j.apgeochem.2013.09.006

Baldeyrou-Bailly, A., Surma, F., Fritz, B., 2004. Geophysical and mineralogical impacts of fluid injection in a geothermal system: the Hot Fractured Rock site at Soultz-sous-Forêts, France. Geological Society, London, Special Publications 236, 355–367. https://doi.org/10.1144/GSL.SP.2004.236.01.20

Barton, N., 2007. Thermal over-closure of joints and rock masses and implications for HLW repositories. Proc. of 11th ISRM Congress 109–116.

Benavente, D., Galiana-Merino, J.J., Pla, C., Martinez-Martinez, J., Crespo-Jimenez, D., 2020. Automatic detection and characterisation of the first P- and S-wave pulse in rocks using ultrasonic transmission method. Engineering Geology 266, 105474. https://doi.org/10.1016/j.enggeo.2020.105474

Benavente, D., García del Cura, M.A., Fort, R., Ordóñez, S., 2004. Durability estimation of porous building stones from pore structure and strength. Engineering Geology 74, 113–127. https://doi.org/10.1016/j.enggeo.2004.03.005

Benavente, D., Lock, P., Ángeles García Del Cura, M., Ordóñez, S., 2002. Predicting the Capillary Imbibition of Porous Rocks from Microstructure. Transport in Porous Media 49, 59–76. https://doi.org/10.1023/A:1016047122877

Benavente, D., Pla, C., Cueto, N., Galvañ, S., Martínez-Martínez, J., García-del-Cura, M.A., Ordóñez, S., 2015. Predicting water permeability in sedimentary rocks from capillary imbibition and pore structure. Engineering Geology 195, 301–311. https://doi.org/10.1016/j.enggeo.2015.06.003

Bérard, T., Cornet, F.H., 2003. Evidence of thermally induced borehole elongation: a case study at Soultz, France. International Journal of Rock Mechanics and Mining Sciences, Special Issue of the IJRMMS: Rock Stress Estimation ISRM Suggested Methods and Associated Supporting Papers 40, 1121–1140. https://doi.org/10.1016/S1365-1609(03)00118-7

Berest, P., Vouille, G., 1988. Notions de base de la thermomécanique : La Thermomécanique des Roches. Manuels et Méthodes, Brgm. ed.

886 Breede, K., Dzebisashvili, K., Liu, X., Falcone, G., 2013. A systematic review of enhanced (or
887 engineered) geothermal systems: past, present and future. Geothermal Energy 1, 4.
888 https://doi.org/10.1186/2195-9706-1-4
889 Cai, J., Yu, B., 2011. A Discussion of the Effect of Tortuosity on the Capillary Imbibition in Porous
890 Media. Transp Porous Med 89, 251–263. https://doi.org/10.1007/s11242-011-9767-0
891 Çelik, M.Y., Kaçmaz, A.U., 2016. The investigation of static and dynamic capillary by water absorption
892 in porous building stones under normal and salty water conditions. Environmental Earth
893 Sciences 75, 307.
894 Chaki, S., Takarli, M., Agbodjan, W.P., 2008. Influence of thermal damage on physical properties of a
895 granite rock: Porosity, permeability and ultrasonic wave evolutions. Construction and
896 Building Materials 22, 1456–1461. https://doi.org/10.1016/j.conbuildmat.2007.04.002
897 Chang, D., Vinegar, H.J., Morriss, C., Straley, C., 1994. Effective Porosity, Producible Fluid And
898 Permeability In Carbonates From Nmr Logging. Presented at the SPWLA 35th Annual Logging
899 Symposium, OnePetro.
900 Cuenot, N., Dorbath, C., Dorbath, L., 2008. Analysis of the Microseismicity Induced by Fluid Injections
901 at the EGS Site of Soultz-sous-Forêts (Alsace, France): Implications for the Characterization of
902 the Geothermal Reservoir Properties. Pure and Applied Geophysics 165, 797–828.
903 https://doi.org/10.1007/s00024-008-0335-7
904 David, C., Menéndez, B., Darot, M., 1999. Influence of stress-induced and thermal cracking on
905 physical properties and microstructure of La Peyratte granite. International Journal of Rock
906 Mechanics and Mining Sciences 36, 433–448. https://doi.org/10.1016/S0148-
907 9062(99)00010-8
908 Dong, Z., Sun, Q., Zhang, W., Xu, C., 2020. Thermal damage of granite after thermal shock cycle.
909 Géotechnique Letters 10, 168–173. https://doi.org/10.1680/jgele.19.00062
910 Drüppel, K., Stober, I., Grimmer, J.C., Mertz-Kraus, R., 2020. Experimental alteration of granitic rocks:
911 Implications for the evolution of geothermal brines in the Upper Rhine Graben, Germany.
912 Geothermics 88, 101903. https://doi.org/10.1016/j.geothermics.2020.101903
913 Dunn, K., LaTorraca, G.A., Bergman, D.J., 1999. Permeability relation with other petrophysical
914 parameters for periodic porous media. GEOPHYSICS 64, 470–478.
915 https://doi.org/10.1190/1.1444552
916 Dwivedi, R.D., Goel, R.K., Prasad, V.V.R., Sinha, A., 2008. Thermo-mechanical properties of Indian
917 and other granites. International Journal of Rock Mechanics and Mining Sciences 45, 303–
918 315. https://doi.org/10.1016/j.ijrmms.2007.05.008
919 Fan, L., Gao, J., Du, X., Wu, Z., 2020. Spatial gradient distributions of thermal shock-induced damage
920 to granite. Journal of Rock Mechanics and Geotechnical Engineering 12, 917–926.
921 https://doi.org/10.1016/j.jrmge.2020.05.004
922 Fan, L.F., Gao, J.W., Wu, Z.J., Yang, S.Q., Ma, G.W., 2018. An investigation of thermal effects on
923 micro-properties of granite by X-ray CT technique. Applied Thermal Engineering 140, 505–
924 519. https://doi.org/10.1016/j.applthermaleng.2018.05.074
925 Farias, P., Gallastegui, G., González Lodeiro, F., Marquínez, J., Martín Parra, L.M., Martínez Catalán,
926 J.R., Pablo Maciá, J. de, Rodríguez Fernández, L.R., 1987. Aportaciones al conocimiento de la
927 litoestratigrafía y estructura de Galicia Central. Memórias da Faculdade de Ciências,
928 Universidade do Porto 1, 411–431.
929 Feng, G., Wang, X., Wang, M., Kang, Y., 2020. Experimental investigation of thermal cycling effect on
930 fracture characteristics of granite in a geothermal-energy reservoir. Engineering Fracture
931 Mechanics 235, 107180. https://doi.org/10.1016/j.engfracmech.2020.107180
932 Fleury, M., 1998. Caractérisation de structures poreuses par relaxométrie RMN. Rev. Inst. Fr. Pét. 53,
933 489–493. https://doi.org/10.2516/ogst:1998041
934 Flores, M., Davies, D.R., Couples, G.D., Palsson, B., 2005. Stimulation of geothermal wells, can we
935 afford it? Presented at the World Geothermal Congress 2005.

936 Fredrich, J.T., Wong, T., 1986. Micromechanics of thermally induced cracking in three crustal rocks.
937 Journal of Geophysical Research: Solid Earth 91, 12743–12764.
938 https://doi.org/10.1029/JB091iB12p12743
939 Freire-Lista, D.M., Fort, R., Varas-Muriel, M.J., 2016. Thermal stress-induced microcracking in
940 building granite. Engineering Geology 206, 83–93.
941 https://doi.org/10.1016/j.enggeo.2016.03.005
942 Fronteau, G., 2000. Comportements télogénétiques des principaux calcaires de Champagne-
943 Ardenne : en relation avec leur facies de dépôt et leur sequençage diagénétique (These de
944 doctorat). Reims.
945 Fronteau, G., Moreau, C., Thomachot-Schneider, C., Barbin, V., 2010. Variability of some Lutetian
946 building stones from the Paris Basin, from characterisation to conservation. Engineering
947 Geology, Natural stones for historical monuments, testing, durability and provenance 115,
948 158–166. https://doi.org/10.1016/j.enggeo.2009.08.001
949 Gautam, P.K., Verma, A.K., Jha, M.K., Sharma, P., Singh, T.N., 2018. Effect of high temperature on
950 physical and mechanical properties of Jalore granite. Journal of Applied Geophysics 159,
951 460–474. https://doi.org/10.1016/j.jappgeo.2018.07.018
952 Géraud, Y., 1994. Variations of connected porosity and inferred permeability in a thermally cracked
953 granite. Geophysical Research Letters 21, 979–982. https://doi.org/10.1029/94GL00642
954 Geraud, Y., Gaviglio, P., 1990. Textural changes in granites submitted to artificial heating: porosity
955 and density variations as functions of the temperature. Comptes Rendus de l'Academie des
956 Sciences. Serie 2 310, 1681–1686.
957 Géraud, Y., Tournier, B., Mazerolle, F., 1999. Detection of porosity and mineralogical variations in
958 geological materials: radiological density measured by CT scan. Proceedings of the
959 International Symposium on Imaging Applications in Geology Geovision 99, 109–112.
960 Glover, P.W.J., Baud, P., Darot, M., Meredith, P.G., Boon, S.A., LeRavalec, M., Zoussi, S., Reuschlé, T.,
961 1995. α/β phase transition in quartz monitored using acoustic emissions. Geophysical
962 Journal International 120, 775–782. https://doi.org/10.1111/j.1365-246X.1995.tb01852.x
963 Gómez-Heras, M., Smith, B.J., Fort, R., 2006. Surface temperature differences between minerals in
964 crystalline rocks: Implications for granular disaggregation of granites through thermal
965 fatigue. Geomorphology 78, 236–249. https://doi.org/10.1016/j.geomorph.2005.12.013
966 Griffiths, L., Lengline, O., Heap, M., Baud, P., Schmittbuhl, J., 2018. Thermal Cracking in Westerly
967 Granite Monitored Using Direct Wave Velocity, Coda Wave Interferometry, and Acoustic
968 Emissions. Journal of Geophysical Research : Solid Earth 123, 2246–2261.
969 https://doi.org/10.1002/2017JB015191
970 Guo, L.-L., Zhang, Y.-B., Zhang, Y.-J., Yu, Z.-W., Zhang, J.-N., 2018. Experimental investigation of
971 granite properties under different temperatures and pressures and numerical analysis of
972 damage effect in enhanced geothermal system. Renewable Energy 126, 107–125.
973 https://doi.org/10.1016/j.renene.2018.02.117
974 Hall, K., André, M.-F., 2003. Rock thermal data at the grain scale: applicability to granular
975 disintegration in cold environments. Earth Surface Processes and Landforms 28, 823–836.
976 https://doi.org/10.1002/esp.494
977 Hammecker, C., Jeannette, D., 1994. Modelling the capillary imbibition kinetics in sedimentary rocks:
978 Role of petrographical features. Transp Porous Med 17, 285–303.
979 https://doi.org/10.1007/BF00613588
980 Hammecker, C., Mertz, J.-D., Fischer, C., Jeannette, D., 1993. A geometrical model for numerical
981 simulation of capillary imbibition in sedimentary rocks. Transp Porous Med 12, 125–141.
982 https://doi.org/10.1007/BF00616976
983 Homand, F., Duffaut, P., Bérest, P., Billaux, D., Boulon, M., Cornet, F., David, C., Durville, J.L., Gentier,
984 S., Giraud, A., Ghoreychi, M., Henry, J.P., Kondo, D., Londe, P., Pellet, F., Piguet, J.P., Sarda,
985 J.P., Shao, J.F., Souley, M., 2000. Manuel de mécanique des roches - tome 1 Fondements,
986 Ecole des Mines de Paris.

Isaka, B.L.A., Gamage, R.P., Rathnaweera, T.D., Perera, M.S.A., Chandrasekharam, D., Kumari, W.G.P., 2018. An Influence of Thermally-Induced Micro-Cracking under Cooling Treatments: Mechanical Characteristics of Australian Granite. Energies 11, 1338. https://doi.org/10.3390/en11061338

Isaka, B.L.A., Ranjith, P.G., Rathnaweera, T.D., Perera, M.S.A., Kumari, W.G.P., 2019. Influence of long-term operation of supercritical carbon dioxide based enhanced geothermal system on mineralogical and microstructurally-induced mechanical alteration of surrounding rock mass. Renewable Energy 136, 428–441. https://doi.org/10.1016/j.renene.2018.12.104

Jin, P., Hu, Y., Shao, J., Zhao, G., Zhu, X., Li, C., 2019. Influence of different thermal cycling treatments on the physical, mechanical and transport properties of granite. Geothermics 78, 118–128. https://doi.org/10.1016/j.geothermics.2018.12.008

Junique, T., Vázquez, P., Géraud, Y., Thomachot-Schneider, C., Sidibé, H., 2021. Microstructural evolution of granitic stones exposed to different thermal regimes analysed by infrared thermography. Engineering Geology 286, 106057. https://doi.org/10.1016/j.enggeo.2021.106057

Kaiser, J., 1953. Erkenntnisse und Folgerungen aus der Messung von Geräuschen bei Zugbeanspruchung von metallischen Werkstoffen. Archiv für das Eisenhüttenwesen 24, 43–45. https://doi.org/10.1002/srin.195301381

Kant, M.A., Ammann, J., Rossi, E., Madonna, C., Höser, D., Rohr, P.R. von, 2017. Thermal properties of Central Aare granite for temperatures up to 500°C: Irreversible changes due to thermal crack formation. Geophysical Research Letters 44, 771–776. https://doi.org/10.1002/2016GL070990

Keating, K., Knight, R., 2006. A laboratory study to determine the effect of iron oxides on proton NMR measurements. GEOPHYSICS 72, E27–E32. https://doi.org/10.1190/1.2399445

Kenyon, B., Kleinberg, R., Straley, C., Gubelin, G., Morriss, C., 1995. Nuclear magnetic resonance imaging - technology for the 21st century. Oilfield Review 7, 19–33.

Kenyon, W.E., Day, P.I., Straley, C., Willemsen, J.F., 1988. A Three-Part Study of NMR Longitudinal Relaxation Properties of Water-Saturated Sandstones. SPE Form Eval 3, 622–636. https://doi.org/10.2118/15643-PA

Kim, K., Kemeny, J., Nickerson, M., 2014. Effect of Rapid Thermal Cooling on Mechanical Rock Properties. Rock Mech Rock Eng 47, 2005–2019. https://doi.org/10.1007/s00603-013-0523-3

Knight, R., Walsh, D.O., Butler, J.J., Grunewald, E., Liu, G., Parsekian, A.D., Reboulet, E.C., Knobbe, S., Barrows, M., 2016. NMR Logging to Estimate Hydraulic Conductivity in Unconsolidated Aquifers. Groundwater 54, 104–114. https://doi.org/10.1111/gwat.12324

Kovač, K., Moore, J., Mcculloch, J., Ekart, D., 2004. Geology and Mineral Paragenesis Study Within the Coso-EGS Project. Presented at the Twenty-Ninth Workshop on Geothermal Reservoir Engineering Stanford University, Stanford, California.

Kumari, W.G.P., Ranjith, P.G., Perera, M.S.A., Chen, B.K., 2018. Experimental investigation of quenching effect on mechanical, microstructural and flow characteristics of reservoir rocks: Thermal stimulation method for geothermal energy extraction. Journal of Petroleum Science and Engineering 162, 419–433. https://doi.org/10.1016/j.petrol.2017.12.033

Kumari, W.G.P., Ranjith, P.G., Perera, M.S.A., Chen, B.K., Abdulagatov, I.M., 2017a. Temperature-dependent mechanical behaviour of Australian Strathbogie granite with different cooling treatments. Engineering Geology 229, 31–44. https://doi.org/10.1016/j.enggeo.2017.09.012

Kumari, W.G.P., Ranjith, P.G., Perera, M.S.A., Shao, S., Chen, B.K., Lashin, A., Arifi, N.A., Rathnaweera, T.D., 2017b. Mechanical behaviour of Australian Strathbogie granite under in-situ stress and temperature conditions: An application to geothermal energy extraction. Geothermics 65, 44–59. https://doi.org/10.1016/j.geothermics.2016.07.002

Lam dos Santos, J.P., Rosa, L.G., Amaral, P.M., 2011. Temperature effects on mechanical behaviour of engineered stones. Construction and Building Materials 25, 171–174. https://doi.org/10.1016/j.conbuildmat.2010.06.042

Lavrov, A., 2003. The Kaiser effect in rocks: principles and stress estimation techniques. International Journal of Rock Mechanics and Mining Sciences 40, 151–171. https://doi.org/10.1016/S1365-1609(02)00138-7

Le Maitre, R.W. (Ed.), 2002. Igneous Rocks: A Classification and Glossary of Terms: Recommendations of the International Union of Geological Sciences Subcommission on the Systematics of Igneous Rocks, 2nd ed. Cambridge University Press, Cambridge. https://doi.org/10.1017/CBO9780511535581

Li, C., Hu, Y., Meng, T., Jin, P., Zhao, Z., Zhang, C., 2020. Experimental study of the influence of temperature and cooling method on mechanical properties of granite: Implication for geothermal mining. Energy Science & Engineering 8, 1716–1728. https://doi.org/10.1002/ese3.627

Lin, W., 2002. Permanent strain of thermal expansion and thermally induced microcracking in Inada granite. Journal of Geophysical Research: Solid Earth 107, ECV 3-1-ECV 3-16. https://doi.org/10.1029/2001JB000648

Liu, C., Deng, H., Wang, Y., Lin, Y., Zhao, H., 2017. Time-Varying Characteristics of Granite Microstructures after Cyclic Dynamic Disturbance Using Nuclear Magnetic Resonance. Crystals 7, 306. https://doi.org/10.3390/cryst7100306

Lutz, S., Robertson-Tait, A., Morris, C., 2004. Stratigraphic relationships in Mesozoic basement rocks at the Desert Peak East EGS area, Nevada. Presented at the Twenty-Ninth Workshop on Geothermal Reservoir Engineering Stanford, University, Stanford, California.

Marshall, V., van Zyl, J., Bryan, S., Uysal, T., Gasparon, M., 2010. Comparative petrology and geochemistry of high heat-producing granites in Australia and Europe, in: Weber, R.D., Gurgenci, H. (Eds.), Proceedings of the 2010 Australian Geothermal Energy Conference. Presented at the Australian Geothermal Energy Conference, Geoscience Australia, Australia, pp. 41–47.

Martínez-Martínez, J., Benavente, D., García-del-Cura, M.A., 2011. Spatial attenuation: The most sensitive ultrasonic parameter for detecting petrographic features and decay processes in carbonate rocks. Engineering Geology 119, 84–95. https://doi.org/10.1016/j.enggeo.2011.02.002

Maurer, J., Knight, R., 2016. Models and methods for predicting hydraulic conductivity in near-surface unconsolidated sediments using nuclear magnetic resonance. GEOPHYSICS 81, D503–D518. https://doi.org/10.1190/geo2015-0515.1

Maurer, V., Gaucher, E., Grunberg, M., Koepke, R., Pestourie, R., Cuenot, N., 2020. Seismicity induced during the development of the Rittershoffen geothermal field, France. Geothermal Energy 8. https://doi.org/10.1186/s40517-020-0155-2

NF EN 1925, 1999. Méthodes d'essai pour pierres naturelles - Détermination du coefficient d'absorption d'eau par capillarité.

NF EN 1936, 2007. Natural stone test methods-Determination of real density and apparent density and of total and open porosity.

Olasolo, P., Juárez, M.C., Morales, M.P., D´Amico, S., Liarte, I.A., 2016. Enhanced geothermal systems (EGS): A review. Renewable and Sustainable Energy Reviews 56, 133–144. https://doi.org/10.1016/j.rser.2015.11.031

Ren, S., Parsekian, A.D., Zhang, Y., Carr, B.J., 2019. Hydraulic Conductivity Calibration of Logging NMR in a Granite Aquifer, Laramie Range, Wyoming. Groundwater 57, 303–319. https://doi.org/10.1111/gwat.12798

Reuschlé, T., Gbaguidi Haore, S., Darot, M., 2006. The effect of heating on the microstructural evolution of La Peyratte granite deduced from acoustic velocity measurements. Earth and Planetary Science Letters 243, 692–700. https://doi.org/10.1016/j.epsl.2006.01.038

1087 Roels, S., Carmeliet, J., Hens, H., Elsen, J., 2000. Microscopic analysis of imbibition processes in oolitic
1088 limestone. Geophysical Research Letters 27, 3533–3536.
1089 https://doi.org/10.1029/1999GL008471
1090 Schmidt, R.B., Bucher, K., Stober, I., 2018. Experiments on granite alteration under geothermal
1091 reservoir conditions and the initiation of fracture evolution. European Journal of Mineralogy
1092 30, 899–916. https://doi.org/10.1127/ejm/2018/0030-2771
1093 Sengun, N., Demirdag, S., Akbay, D., Ugur, I., Altindag, R., Akbulut, A., 2014. Investigation of the
1094 relationships between capillary water absorption coefficients and other rock properties of
1095 some natural stones, V, in: Global Stone Congress. pp. 22–25.
1096 Sepúlveda, J., Arancibia, G., Molina, E., Gilbert, J.P., Duda, M., Browning, J., Roquer, T., Morata, D.,
1097 Ahrens, B., Bracke, R., 2020. Thermo-mechanical behavior of a granodiorite from the Liquiñe
1098 fractured geothermal system (39°S) in the Southern Volcanic Zone of the Andes.
1099 Geothermics 87, 101828. https://doi.org/10.1016/j.geothermics.2020.101828
1100 Sha, S., Rong, G., Chen, Z., Li, B., Zhang, Z., 2020. Experimental Evaluation of Physical and Mechanical
1101 Properties of Geothermal Reservoir Rock after Different Cooling Treatments. Rock Mech
1102 Rock Eng 53, 4967–4991. https://doi.org/10.1007/s00603-020-02200-5
1103 Shao, S.S., Wasantha, P.L., Ranjith, P.G., Chen, B., 2014. Effect of cooling rate on the mechanical
1104 behavior of heated Strathbogie granite with different grain sizes. International Journal of
1105 Rock Mechanics & Mining Sciences 70, 381–387.
1106 https://doi.org/10.1016/j.ijrmms.2014.04.003
1107 Shen, Y., Hou, X., Yuan, J., Xu, Z., Hao, J., Gu, L., Liu, Z., 2020. Thermal deterioration of high-
1108 temperature granite after cooling shock: multiple-identification and damage mechanism.
1109 Bull Eng Geol Environ 79, 5385–5398. https://doi.org/10.1007/s10064-020-01888-7
1110 Siratovich, P., Sass, I., Homuth, S., Bjornsson, A., 2011. Thermal Stimulation of Geothermal
1111 Reservoirs and Laboratory Investigation of Thermally Induced Fractures. Transactions -
1112 Geothermal Resources Council 35, 1529–1535.
1113 Siratovich, P.A., Heap, M.J., Villeneuve, M.C., Cole, J.W., Kennedy, B.M., Davidson, J., Reuschlé, T.,
1114 2016. Mechanical behaviour of the Rotokawa Andesites (New Zealand): Insight into
1115 permeability evolution and stress-induced behaviour in an actively utilised geothermal
1116 reservoir. Geothermics 64, 163–179. https://doi.org/10.1016/j.geothermics.2016.05.005
1117 Siratovich, P.A., Villeneuve, M.C., Cole, J.W., Kennedy, B.M., Bégué, F., 2015. Saturated heating and
1118 quenching of three crustal rocks and implications for thermal stimulation of permeability in
1119 geothermal reservoirs. International Journal of Rock Mechanics and Mining Sciences 80,
1120 265–280. https://doi.org/10.1016/j.ijrmms.2015.09.023
1121 Sousa, L.M.O., Suárez del Río, L.M., Calleja, L., Ruiz de Argandoña, V.G., Rey, A.R., 2005. Influence of
1122 microfractures and porosity on the physico-mechanical properties and weathering of
1123 ornamental granites. Engineering Geology 77, 153–168.
1124 https://doi.org/10.1016/j.enggeo.2004.10.001
1125 Straley, C., Rossini, D., Vinegar, H., Tutunjian, P., Morriss, C., 1997. Core Analysis By Low-field Nmr.
1126 The Log Analyst 38.
1127 Stussi, J.-M., Cheilletz, A., Royer, J.-J., Chervremont, P., Feraud, G., 2002. The hidden monzogranite
1128 of Soultz-sous-Forêts (Rhine Graben, France). Mineralogy, petrology and genesis. Géol. Fr
1129 45–64.
1130 Surma, F., Geraud, Y., 2003. Porosity and Thermal Conductivity of the Soultz-sous-Forêts Granite.
1131 Pure appl. geophys. 160, 1125–1136. https://doi.org/10.1007/PL00012564
1132 Takarli, M., Prince-Agbodjan, W., 2008. Temperature Effects on Physical Properties and Mechanical
1133 Behavior of Granite: Experimental Investigation of Material Damage. JAI 5, 1–13.
1134 https://doi.org/10.1520/JAI100464
1135 Tang, Z.C., Sun, M., Peng, J., 2019. Influence of high temperature duration on physical, thermal and
1136 mechanical properties of a fine-grained marble. Applied Thermal Engineering 156, 34–50.
1137 https://doi.org/10.1016/j.applthermaleng.2019.04.039

Tarasovs, S., Ghassemi, A., 2012. On the role of thermal stress in reservoir stimulation. Proceedings: Thirty-Seventh Workshop on Geothermal Reservoir Engineering.
Tian, W.-L., Yang, S.-Q., Elsworth, D., Wang, J.-G., Li, X.-Z., 2020. Permeability evolution and crack characteristics in granite under treatment at high temperature. International Journal of Rock Mechanics and Mining Sciences 134, 104461. https://doi.org/10.1016/j.ijrmms.2020.104461
Ueda, A., Kato, K., Ohsumi, T., Yajima, T., Ito, H., Kaieda, H., Metcalfe, R., Takase, H., 2005. Experimental studies of CO2-rock interaction at elevated temperatures under hydrothermal conditions. Geochemical Journal 39, 417–425. https://doi.org/10.2343/geochemj.39.417
Vazquez, P., Carrizo, L., Thomachot-Schneider, C., Gibeaux, S., Alonso, F.J., 2016. Influence of surface finish and composition on the deterioration of building stones exposed to acid atmospheres. Construction and Building Materials 106, 392–403. https://doi.org/10.1016/j.conbuildmat.2015.12.125
Vazquez, P., Sánchez-Delgado, N., Carrizo, L., Thomachot-Schneider, C., Alonso, F.J., 2018. Statistical approach of the influence of petrography in mechanical properties and durability of granitic stones. Environ Earth Sci 77, 287. https://doi.org/10.1007/s12665-018-7475-6
Vazquez, P., Shushakova, V., Gómez-Heras, M., 2015. Influence of mineralogy on granite decay induced by temperature increase: Experimental observations and stress simulation. Engineering Geology 189, 58–67. https://doi.org/10.1016/j.enggeo.2015.01.026
Vazquez, P., Siegesmund, S., Alonso, F.J., 2011. Bowing of dimensional granitic stones. Environ Earth Sci 63, 1603–1612. https://doi.org/10.1007/s12665-010-0882-y
Vera, J.A., 2004. Geología de España. SGE-IGME.
Weng, L., Wu, Z., Li, X., 2018. Mesodamage Characteristics of Rock with a Pre-cut Opening Under Combined Static–Dynamic Loads: A Nuclear Magnetic Resonance (NMR) Investigation. Rock Mech Rock Eng 51, 2339–2354. https://doi.org/10.1007/s00603-018-1483-4
Wogelius, R.A., Milodowski, A.E., Field, L.P., Metcalfe, R., Lowe, T., van Veelen, A., Carpenter, G., Norris, S., Yardley, B., 2020. Mineral reaction kinetics constrain the length scale of rock matrix diffusion. Scientific Reports 10, 8142. https://doi.org/10.1038/s41598-020-65113-x
Wu, Q., Weng, L., Zhao, Y., Guo, B., Luo, T., 2019. On the tensile mechanical characteristics of fine-grained granite after heating/cooling treatments with different cooling rates. Engineering Geology 253, 94–110. https://doi.org/10.1016/j.enggeo.2019.03.014
Xu, C., Sun, Q., 2018. Effects of quenching cycle on tensile strength of granite. Géotechnique Letters 8, 165–170. https://doi.org/10.1680/jgele.18.00053
Xu, X., Gao, F., Shen, X., Xie, H., 2008. Mechanical characteristics and microcosmic mechanisms of granite under temperature loads. Journal of China University of Mining and Technology 18, 413–417. https://doi.org/10.1016/S1006-1266(08)60086-3
Yilmaz, N., Karaca, Z., Goktan, R.M., Akal, C., 2009. Relative brittleness characterization of some selected granitic building stones: Influence of mineral grain size. Construction and Building Materials 23, 370–375. https://doi.org/10.1016/j.conbuildmat.2007.11.014
Yong, C., Wang, C., 1980. Thermally induced acoustic emission in westerly granite. Geophysical Research Letters 7, 1089–1092. https://doi.org/10.1029/GL007i012p01089
Yu, P., Pan, P.-Z., Feng, G., Wu, Z., Zhao, S., 2020. Physico-mechanical properties of granite after cyclic thermal shock. Journal of Rock Mechanics and Geotechnical Engineering 12, 693–706. https://doi.org/10.1016/j.jrmge.2020.03.001
Yun, T.S., Jeong, Y.J., Kim, K.Y., Min, K.-B., 2013. Evaluation of rock anisotropy using 3D X-ray computed tomography. Engineering Geology 163, 11–19. https://doi.org/10.1016/j.enggeo.2013.05.017
Zeng, Y., Tang, L., Wu, N., Cao, Y., 2017. Analysis of influencing factors of production performance of enhanced geothermal system: A case study at Yangbajing geothermal field. Energy 127, 218–235. https://doi.org/10.1016/j.energy.2017.03.100

Zhang, F., Zhao, J., Hu, D., Skoczylas, F., Shao, J., 2018. Laboratory Investigation on Physical and Mechanical Properties of Granite After Heating and Water-Cooling Treatment. Rock Mech Rock Eng 51, 677–694. https://doi.org/10.1007/s00603-017-1350-8

Zhang, W., Sun, Q., Zhang, Y., Xue, L., Kong, F., 2018. Porosity and wave velocity evolution of granite after high-temperature treatment: a review. Environ Earth Sci 77, 350. https://doi.org/10.1007/s12665-018-7514-3

Zhao, Yangsheng, Feng, Z., Zhao, Yu, Wan, Z., 2017. Experimental investigation on thermal cracking, permeability under HTHP and application for geothermal mining of HDR. Energy 132, 305–314. https://doi.org/10.1016/j.energy.2017.05.093

Zhou, C., Remoroza, A.I., Shah, K., Doroodchi, E., Moghtaderi, B., 2016. Experimental study of static and dynamic interactions between supercritical CO2/water and Australian granites. Geothermics 64, 246–261. https://doi.org/10.1016/j.geothermics.2016.05.007

Zhu, Z., Tian, H., Chen, J., Jiang, G., Dou, B., Xiao, P., Mei, G., 2020. Experimental investigation of thermal cycling effect on physical and mechanical properties of heated granite after water cooling. Bull Eng Geol Environ 79, 2457–2465. https://doi.org/10.1007/s10064-019-01705-w